

AD-A182 575

ANALYSIS OF SOLID STATE PLASMA FORMATION IN
SEMICONDUCTOR COMPONENTS(U) AIR FORCE WEAPONS LAB
KIRTLAND AFB NM M SNYDER ET AL MAR 86 AFML-TR-85-116
F/G 28/3

1/1

UNCLASSIFIED

NL

END
1/1
1/1



DTIC FILE COPY

2

AD-A182 575

ANALYSIS OF SOLID STATE PLASMA FORMATION IN SEMICONDUCTOR COMPONENTS

Captain Mark Snyder
Dr Howard Volkin

April 1987

DTIC
ELECTE
JUN 26 1987
S D
D R

Final Report

Approved for public release; distribution unlimited.

AIR FORCE WEAPONS LABORATORY
Air Force Systems Command
Kirtland Air Force Base, NM 87117-6008

This final report was prepared by the Air Force Weapons Laboratory, Kirtland Air Force Base, New Mexico under Job Order ILIR8421. William R. Ayres (NTA) was the Laboratory Project Officer-in-Charge.

When Government drawings, specifications, or other data are used for any purpose other than in connection with a definitely Government-related procurement, the United States Government incurs no responsibility or any obligation whatsoever. The fact that the Government may have formulated or in any way supplied the said drawings, specifications, or other data, is not to be regarded by implication, or otherwise in any manner construed, as licensing the holder, or any other person or corporation; or as conveying any rights or permission of manufacture, use or sell any patented invention that may in any way be related thereto.

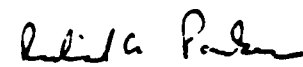
This report has been authored by an employee of the United States Government. Accordingly, the United States Government retains a nonexclusive, royalty-free license to publish or otherwise reproduce the material contained herein, or allow others to do so, for United States Government purposes.

This report has been reviewed by the Public Affairs Office and is releasable to the National Technical Information Service (NTIS). At NTIS, it will be available to the general public, including foreign nations.

If your address has changed, if you wish to be removed from our mailing list, or if your organization no longer employs the addressee, please notify AFWL/NTA, Kirtland AFB, NM 87117-6008 to help us maintain a current mailing list.

This technical report has been reviewed and is approved for publication.


WILLIAM R. AYRES
Project Officer


RICHARD A. PAULSEN
Captain, USAF
Chief, Technology Branch

FOR THE COMMANDER


PHILIP J. MESSURI
Major, USAF
Chief, Aircraft & Missile Division

DO NOT RETURN COPIES OF THIS REPORT UNLESS CONTRACTUAL OBLIGATIONS OR NOTICE ON A SPECIFIC DOCUMENT REQUIRES THAT IT BE RETURNED.

UNCLASSIFIED

SECURITY CLASSIFICATION OF THIS PAGE

ADP 182 575

REPORT DOCUMENTATION PAGE

1a. REPORT SECURITY CLASSIFICATION UNCLASSIFIED		1b. RESTRICTIVE MARKINGS	
2a. SECURITY CLASSIFICATION AUTHORITY		3. DISTRIBUTION/AVAILABILITY OF REPORT Approved for public release; distribution unlimited.	
2b. DECLASSIFICATION/DOWNGRADING SCHEDULE			
4. PERFORMING ORGANIZATION REPORT NUMBER(S) AFWL-TR-85-116		5. MONITORING ORGANIZATION REPORT NUMBER(S)	
6a. NAME OF PERFORMING ORGANIZATION Air Force Weapons Laboratory	6b. OFFICE SYMBOL (If applicable) NTA	7a. NAME OF MONITORING ORGANIZATION	
6c. ADDRESS (City, State and ZIP Code) Kirtland Air Force Base, NM 87117-6008		7b. ADDRESS (City, State and ZIP Code)	
8a. NAME OF FUNDING SPONSORING ORGANIZATION	8b. OFFICE SYMBOL (If applicable)	9. PROCUREMENT INSTRUMENT IDENTIFICATION NUMBER	
8c. ADDRESS (City, State and ZIP Code)		10. SOURCE OF FUNDING NOS	
		PROGRAM ELEMENT NO. 61101F	PROJECT NO. ILIR
		TASK NO. 84	WORK UNIT NO. 21
11. TITLE (Include Security Classification) ANALYSIS OF SOLID STATE PLASMA FORMATION IN SEMICONDUCTOR COMPONENTS			
12. PERSONAL AUTHOR(S) Snyder, Captain Mark; and Volkin, Dr Howard			
13a. TYPE OF REPORT Final	13b. TIME COVERED FROM Dec 83 TO May 85	14. DATE OF REPORT (Yr., Mo., Day) 1986 March	15. PAGE COUNT 94
16. SUPPLEMENTARY NOTATION			
17. COSATI CODES		18. SUBJECT TERMS (Continue on reverse if necessary and identify by block number)	
FIELD	GROUP	SUB. GR.	
20	12		Solid state plasma
09	02		Failure mechanisms
			Semiconductor
19. ABSTRACT (Continue on reverse if necessary and identify by block number) A study is performed to determine the physical mechanism responsible for the destruction of semiconductor components exposed to intense optical or electric fields. This paper suggests that solid state plasma formation is the responsible mechanism. Proof is provided via theoretical analysis and experimental data to show solid state plasma formation comes about due to the quantum mechanical aspects of semiconductors. To capitalize on this thesis, work began to construct an ensemble Monte Carlo program to model plasma effects under intense optical or electrical illumination in four semiconductor materials.			
20. DISTRIBUTION/AVAILABILITY OF ABSTRACT UNCLASSIFIED/UNLIMITED <input checked="" type="checkbox"/> SAME AS RPT <input type="checkbox"/> DTIC USERS <input type="checkbox"/>		21. ABSTRACT SECURITY CLASSIFICATION UNCLASSIFIED	
22a. NAME OF RESPONSIBLE INDIVIDUAL WILLIAM R. AYRES		22b. TELEPHONE NUMBER (Include Area Code) (505) 844-9758	22c. OFFICE SYMBOL NTA

CONTENTS

<u>Section</u>		<u>Page</u>
1.0	INTRODUCTION	1
2.0	BACKGROUND OF THE PROBLEM	3
3.0	THE SOLID STATE PLASMA	5
	3.1 DEFINITION AND CRITERIA	5
	3.2 COMPENSATED PLASMAS	11
	3.3 UNCOMPENSATED PLASMAS	11
	3.4 UNCOMPENSATED MULTICOMPONENT PLASMAS	11
	3.5 NONEQUILIBRIUM PLASMAS	12
4.0	EQUILIBRIUM AND INSTABILITIES IN PLASMAS	13
	4.1 STREAMING INSTABILITIES	13
	4.2 RAYLEIGH-TAYLOR INSTABILITIES	13
	4.3 KINEMATIC INSTABILITIES	14
	4.4 UNIVERSAL INSTABILITIES	14
5.0	DEVICE AND MATERIAL FAILURE	15
6.0	FILAMENTATION DUE TO PINCH	17
	6.1 THE BENNETT PINCH	17
	6.2 THE EQUILIBRIUM PINCH	17
	6.3 THE DYNAMIC PINCH	30
7.0	GROWTH INSTABILITIES OF THE EQUILIBRIUM SOLID STATE PLASMA	31
	7.1 SAUSAGE INSTABILITY	31
	7.2 KINK INSTABILITY	34
	7.3 STREAMING INSTABILITIES	34
8.0	THERMAL PINCH	39
9.0	MONTE CARLO METHOD	43
	9.1 NUMERICAL ANALYSIS OF SEMICONDUCTOR DEVICES	46
	9.2 QUASI-CLASSICAL DESCRIPTION OF CHARGE TRANSPORT	48
	9.3 MONTE CARLO SIMULATION	50
	9.4 ENSEMBLE MONTE CARLO	51
	9.5 ENERGY BAND STRUCTURE	53
	9.6 REALISTIC BAND STRUCTURE	55
	9.7 SCATTERING RATES	55
	9.8 QUANTUM EFFECTS	57
	9.9 TIME-OF-FLIGHT ALGORITHMS	58
	9.10 COLLECTIVE EFFECTS	60
	9.11 NEGATIVE DIFFERENTIAL CONDUCTIVITY	63

CONTENTS (Concluded)

<u>Section</u>		<u>Page</u>
10.0	MONTE CARLO ANALYSES AT VERY HIGH FIELDS	65
10.1	RESULTS FOR ITEM 1	66
10.2	RESULTS FOR ITEM 2	66
10.3	RESULTS FOR ITEM 3	66
10.4	RESULTS FOR ITEM 4	66
	REFERENCES	67
	APPENDIX	69

1.0 INTRODUCTION

The scientific community has exploited the unique capabilities of semiconductors to produce various kinds of electrical and optical components. However, the increasing energy levels these components are required to handle are quickly surpassing the materials' stable energy handling capabilities. Research continues to expand the known stable energy handling modes of semiconductors. Still, the question arises: At what energy level or under what conditions do unstable energy handling modes occur for semiconductors?

Yet, this question reveals a deeper dilemma upon examination. Numerous efforts have approached this problem utilizing very simple experiments and a priori failure concepts to obtain an understanding of failure phenomena associated with unstable energy handling modes that can be applied to more complex situations. In general, this type of approach has been thwarted by the appearance of failure phenomena (Ref. 1) that are not consistent with simple theories (Ref. 1). It is apparent that such results, from simple experiments, point to a more complex mechanism that may be discernable under more sophisticated modeling techniques.

Ensemble Monte Carlo simulation of semiconductor carrier transport has consistently improved over the last decade to the point of achieving excellent agreement with experiments. Thus, this state-of-the-art tool is the vehicle upon which this effort will work to achieve its objective: The modeling of carrier transport in semiconductors under high optical or electric field conditions to determine the physical mechanisms involved in, or triggering, unstable modes of carrier transport.

To develop this capability at the Air Force Weapons Laboratory (AFWL) without outside help would be a major project requiring a large number of man-hours and computer time. Therefore, the decision was made to acquire the basic Monte Carlo program and upgrade the code from there.

The primary source for the computer code was from North Carolina State University. This program, authored by Dr M.A. Littlejohn and Dr J. Hauser, is the basis used by all state-of-the-art semiconductor Monte Carlo simulations and is the basis upon which this effort will build.

Simulation results were obtained via the ensemble Monte Carlo program operated by Dr Karl Hess at the University of Illinois at Urbana, Illinois. This program is the most advanced simulation of its type in the world and provides check cases for this studies code development and modeling effort.

Dr Howard Volkin was responsible for this efforts code upgrading and running.

Interpretation of program results were directly aided by Lt Mark Snyder, AFWL/NTAT; Dr Erick Kunhardt of Brooklyn Polytechnical Institute and Dr William Portnoy of Texas Tech University.

2.0 BACKGROUND OF THE PROBLEM

This study was initiated by the results enumerated in References 1, 2 and 3 as applied to finding the physical mechanisms involved in semiconductor device failure due to an electrical overstress. These studies found the collective behavior, known as second breakdown, that occurs in semiconductor devices exposed to an electrical overstress was the result of the formation of an unstable solid state plasma. Formation of the plasma occurred due to the transition from single-carrier to double-carrier current injection or from the excitation of carriers into the upper conduction bands forming a single-carrier plasma dominated by a particular conduction minima. In principle, the physical mechanisms associated with plasma formation were found to have a strong dependence on the specific material band structure, and device architecture. Modeling a semiconductor material (without a device structure) for single- to double-carrier injection could be performed for specific cases analytically, but higher order band structure effects can only be dealt with on a fully quantum mechanical level. Thus, a Monte Carlo simulation utilizing a quantum mechanical representation of the crystalline lattice (called the pseudopotential method) was seen as the only alternative to pursue.

Additional experimental evidence for plasma formation was found on examination of laser-induced electric breakdown in solids. Bloemberger (Ref. 4) states that laser-induced electron avalanche is usually the mechanism that determines the failure threshold in pure solids. Multiphoton ionization of electrons leads to the formation of a cloud of electrons that become opaque to the laser and thus highly absorptive, leading to thermal failure.

This physical process is reported by Bloemberger to be responsible for failure at the surface as well as in the bulk of a material. Yet, this may be true only if physical and chemical defects are not prevalent in the material.

The concept of failure put forth for laser-induced electric breakdown is similar to the concept presently used to explain electrically stressed failure of materials. A common scenario would be as follows: A material is stressed by an electric field (optically or electrically) initiating carrier production and movement. If the field is increased in magnitude, impact ionization will occur forming double-carrier injection (also known as avalanche injection).

As the number of carriers increase with further impact ionization, a point is reached where the kinetic energy of the carriers is efficiently imparted to the material lattice resulting in joule heating. The joule heating increases the kinetic energy and number of carriers involved in impact ionization forming a positive feedback cycle (or runaway effect). If not checked, this feedback cycle increases with time until thermal shock occurs.

Closer examination of experimental work in device failure (Ref. 1) shows direct evidence of fine structure in the carrier cloud formed from intense avalanche injection. This evidence shows isotropic device current collapsing to filamentary structures which grow and destroy a device by thermal shock. Current-voltage characteristics associated with failure also exhibit a fine structure that is not descriptive of currently known device physics. Thus, this explanation of material failure (avalanche leading to runaway) is not an entirely accurate representation of the failure phenomena observed.

Various theories have attempted to explain the fine structure observed but most have failed to explain the general aspects under which failure occurs; i.e., formation of current filaments.

This study will attempt to simulate the general aspects occurring when a semiconductor material is exposed to high amplitude electromagnetic fields from an electrical or optical overstress. Particular attention will be paid to those aspects that may lead to the formation of a solid state plasma.

3.0 THE SOLID STATE PLASMA

3.1 DEFINITION AND CRITERIA

A plasma is generally defined as an ionized gas of electronically quasi-neutral particles that exhibit a collective behavior in reaction to the surrounding environment (Ref. 5). The term quasi-neutral refers to a neutrality that occurs due to the kinetic action of the particles forming an electrostatic shielding effect between like charges. This is known as Debye shielding and forms a critical concept necessary to the definition of a plasma. The term "collective behavior" describes how a plasma reacts as a single entity to the surrounding environment. Individual carrier movement in a plasma is not readily discernable at the microscopic level due to Debye shielding, and plasma reaction to an outside force is dominated by the need to sustain equilibrium and keep the plasma free of electric potentials or fields. The only way to maintain these requirements is by reacting as a single unit.

Criteria have been developed to provide proof of a plasma state according to the above definitions. The first criterion deals with the Debye length or thickness of the Debye shielding around a charged carrier. The Debye length is defined as

$$\lambda_D \equiv \left(\frac{kT_e \epsilon}{4\pi n e^2} \right)^{\frac{1}{2}} \ll \text{the system's dimensions.} \quad (1)$$

where

k = Boltzmann's constant
 T = carrier temperature
 n = carrier density
 e = electronic charge
 ϵ = dielectric constant

Under this criterion, the Debye length must be much smaller than the dimensions of the system containing the plasma.

This criterion gives rise to a second criterion based on the premise that if the Debye length is much smaller than the system's dimensions, a sufficient number of carriers should exist within a Debye sphere to provide shielding, or

$$N_D = n \frac{4}{3} \pi \lambda_D^3 \gg 1 \quad (2)$$

where

N_D = number of particles within a Debye sphere
 n = carrier density
 λ_D = Debye length

A final criterion deals with the plasma's ability to possess collective behavior that is not swamped out by random collisions. To fulfill this criterion, the frequency of an oscillation (ω) in the plasma times the mean time between collisions (τ) must be greater than one, or

$$\omega\tau > 1 \quad (3)$$

These three criteria must be met in order to define an ionized gas of carriers as a plasma. Does the carrier transport in a semiconductor possess the qualities necessary to fulfill the above criteria to be called a plasma? The answer is yes, as demonstrated in the following.

A semiconductor's material is capable of transporting a charge in accordance with the basic principles of quantum mechanics. The crystalline potentials that make up the background for charge transport influence carrier motion via quantum mechanics in such a way as to impart an effective mass (Ref. 6) that is greatly reduced from the carrier's rest mass (Ref. 6).

The crystal potential is not a constant -- it is a tensor and changes with orientation of the crystalline lattice to the applied field. Therefore, the effective mass is a tensor. The crystal potential also varies in terms of the energy. Thus, a carrier at 2 eV will view the lattice differently than a carrier at 1.5 eV. The aspects of a plasma composed of 2 eV carriers are different than those of a plasma of 1.5 eV carriers. But how are these plasma aspects determined? And how is it known that a solid state plasma exists?

The carrier population in a semiconductor can take on the aspects of a plasma due to the Heisenberg uncertainty principle

$$\Delta p \Delta x \geq \frac{h}{4\pi} \quad (4)$$

where

Δp = uncertainty in linear momentum.
 Δx = uncertainty in position.
 h = Planck's constant = 6.62×10^{-27} erg-sec.

The temperature of carriers in a solid is related to the carriers' kinetic energy by

$$\frac{3}{2}kT \doteq \frac{1}{2}m \langle v^2 \rangle$$

or

$$T \doteq \frac{m \langle v^2 \rangle}{3k} = \frac{\langle p^2 \rangle}{3km} \quad (5)$$

where

- k = Boltzmann's constant.
- T = carrier temperature.
- m = carrier mass.
- $\langle v^2 \rangle$ = average of the carrier velocity squared.

As the number of carriers increase, Δx decreases, Δp increases, and the carriers' temperatures increase.

The intrinsic carrier concentration in a semiconductor will give a rough estimate of the average distance between carriers by $\Delta x \approx n_i^{-1/3}$. Equation 4 now becomes

$$\Delta p \geq \frac{h n_i^{1/3}}{4\pi} \quad (6)$$

and Equation 5 becomes

$$T \geq \left(\frac{h n_i^{1/3}}{4\pi} \right)^2 \frac{1}{3km^*} \quad (7)$$

The carrier mass (m^*) in Equation 7 is the effective mass for a particular material. Here, this quantity is treated as a magnitude as long as the majority of carrier movement is along one crystal orientation only. The effective mass for most semiconductors is only a fraction of the carrier's rest mass (Ref. 7). Thus, a small effective mass and large carrier concentration can create a large carrier temperature, as shown in Table 1.

TABLE 1. THE UNITS FOR THE EFFECTIVE MASSES (i.e. m_e^* , m_{hh}^* and m_{lh}^*) ARE IN GRAMS. THE SUBSCRIPTS STAND FOR ELECTRON, HEAVY HOLE, AND LIGHT HOLE RESPECTIVELY. THE TEMPERATURES ARE IN KELVIN. NO APPLIED FIELD.

	$n(\text{cm}^{-3})$	m_e^*	m_{hh}^*	m_{lh}^*	T_e	T_{hh}	T_{lh}
InSb	1×10^{17}	0.015	0.39	0.021	10.6	0.40	7.5
GaAs	1×10^{14}	0.07	0.68	0.12	2.3×10^{-2}	2.3×10^{-3}	1.3×10^{-2}
	1×10^{18}	0.07	0.68	0.12	10.5	1.08	6.14
N-Ge	1×10^{15}	0.12	0.34	0.043	6.1×10^{-2}	2.1×10^{-2}	0.17
	1×10^{18}	0.12	0.34	0.043	6.14	2.16	17.1
N-Si	1×10^{14}	0.26	0.52	0.16	6.1×10^{-3}	3×10^{-3}	1×10^{-2}
	1×10^{18}	0.26	0.52	0.16	2.83	1.41	4.6

The values obtained through Equation 1 for Debye lengths will increase with increased carrier concentration and carrier temperature and possess values as follows in Table 2.

TABLE 2. CALCULATED DEBYE LENGTHS FOR THE TEMPERATURES DETAILED IN TABLE 1.

	$n(\text{cm}^{-3})$	Debye Lengths (in cm)		
		e	hh	lh
InSb	1×10^{17}	2.92×10^{-7}	5.7×10^{-8}	2.4×10^{-7}
GaAs	1×10^{14}	5.5×10^{-7}	1.2×10^{-7}	2.75×10^{-7}
	1×10^{18}	7.7×10^{-8}	2.5×10^{-8}	2.7×10^{-7}
N-Ge	1×10^{15}	2.16×10^{-7}	1.2×10^{-7}	3.8×10^{-7}
	1×10^{18}	6.8×10^{-8}	4×10^{-8}	1.2×10^{-7}
N-Si	1×10^{14}	1.9×10^{-7}	1.3×10^{-7}	2.4×10^{-7}
	1×10^{18}	4.1×10^{-8}	2.8×10^{-8}	5.12×10^{-8}

These values can be inserted in Equation 2 to determine if the Debye shielding is effective (Table 3).

TABLE 3. NUMBER OF CARRIERS CONTAINED IN DEBYE SPHERE FOR THE TEMPERATURES DETAILED IN TABLE 1. NO APPLIED FIELD.

	Number of carriers within a Debye Sphere (cm^{-3})			
	$n(\text{cm}^{-3})$	N_{De}	N_{Dhh}	N_{DLh}
InSb	1×10^{17}	1.0×10^{-2}	7.8×10^{-5}	5.7×10^{-3}
GaAs	1×10^{14}	1.8×10^{-5}	7.2×10^{-7}	8.7×10^{-6}
	1×10^{18}	1.9×10^{-3}	6.5×10^{-5}	8.2×10^{-2}
N-Ge	1×10^{15}	4.2×10^{-5}	7.2×10^{-6}	1.9×10^{-4}
	1×10^{18}	1.3×10^{-3}	2.6×10^{-4}	7.2×10^{-3}
N-Si	1×10^{14}	2.9×10^{-6}	9.2×10^{-7}	5.8×10^{-6}
	1×10^{18}	2.8×10^{-4}	9.2×10^{-5}	5.6×10^{-4}

These tables show that many semiconductors do not fulfill all of the requirements for a plasma without an external field -- the number of carriers within a Debye radius are insufficient to shield a carrier from external electromagnetic forces.

Equation 3 is the final criterion to determine plasma formation. This equation represents the quality of the plasma, or sharpness of the plasma oscillations. If the plasma oscillations are heavily damped by collisions, the plasma is not well formed and reacts sluggishly to external forces. The types of collisions that occur in a semiconductor must be examined to determine the sharpness of a solid state plasma.

Collisions in a semiconductor fall under three different categories: (1) collisions with the lattice, (2) collisions with other carriers, and (3) carrier scattering by phonons (lattice vibrations). Collisions with the lattice are of prime concern when the lattice captures carriers through stationary traps or defects. This action limits the carrier's lifetime or ability to contribute to carrier flow in the material. Lifetime is dependent on trap density, free-carrier density and carrier energy. Collisions with other carriers is not important until the carrier density and energy are extremely large. Phonon interaction is only important when carrier energy is relatively high compared to room temperature. Thus, under the conditions of small external

fields or temperature gradients, the lifetime gives the best approximation of the time between collisions.

The ability of a material to react to an electromagnetic wave is measured as a function of the material's dielectric relaxation time. The relaxation time is the time needed for a material to redistribute carriers to maintain electrical neutrality (Ref. 8).

The dielectric relaxation time also determines the plasma frequency of the material; i.e., the frequency above which electromagnetic waves can be transmitted in a free-carrier medium according to dispersion relations. The relaxation time τ_r is found from the following equation

$$\tau_r = \left(\frac{\epsilon m^*}{4\pi n e^2} \right)^{1/2} \quad (8)$$

where

- ϵ = relative permittivity times the free space permittivity
- m^* = effective carrier mass
- n = free carrier density

This equation yields values for the materials listed in Table 4.

TABLE 4. PLASMA FREQUENCY CALCULATED FROM THE DIELECTRIC RELAXATION TIME FOR EACH MATERIAL.

	Plasma Frequency	
	n (cm^{-3})	(hertz)
InSb	1×10^{17}	3.53×10^{13}
GaAs	1×10^{14}	6.03×10^{11}
	1×10^{18}	6.03×10^{13}
N-Ge	1×10^{15}	1.28×10^{12}
	1×10^{18}	4.07×10^{13}
N-Si	1×10^{14}	3.19×10^{11}
	1×10^{18}	3.19×10^{13}

The calculated plasma frequencies show that plasma reaction (thus sharpness of oscillation) is much faster than the time needed (≈ 1 ns) to capture carriers at traps in the lattice. Thus, situations can arise in semiconductors where most of the criteria for definition of plasma can be met with no injection effects. This discussion does not imply that solid state plasma exist under all conditions. However, the basic criteria should be rechecked under different physical conditions to insure compliance.

Application of an electric field, optical field, or external heating can raise the velocity of carriers to extremely high levels ($\approx 1 \times 10^7$ cm/s) with a correspondingly high temperature (≈ 200 K), a larger Debye length ($\approx 1 \times 10^{-5}$ cm), and a larger N (≈ 5). The preceding tables and the figures in the Appendix show that a solid state plasma can satisfy the same criteria of other well known plasma forms.

Applying the principles put forth on the preceding pages to more specific cases results in the description of three different kinds of solid state plasmas depending on the quantity of carriers and type of doping.

3.2 COMPENSATED PLASMAS

A compensated solid state plasma contains equal numbers of mobile electrons and holes. This type of plasma is likely to occur under intrinsic material conditions at low level injection regimes. The occurrence of avalanche breakdown in a semiconductor may form the conditions for a compensated plasma, if the material's band structure does not play an exceedingly important role. This type of plasma can be weakly or strongly ionized (a large or small carrier temperature).

3.3 UNCOMPENSATED PLASMAS

This plasma forms in doped semiconductors where the concentration of mobile electrons and holes are unequal. The majority of mobile charges are compensated for by stationary donor or acceptor sites in the crystalline lattice. The majority carrier density under these circumstances is relatively high and makes formation of a plasma easy. This type of plasma will be predominant in semiconductor devices, especially under high-level injection regimes.

3.4 UNCOMPENSATED MULTICOMPONENT PLASMAS

Once free-carrier energies are high enough to reach the upper conduction bands of semiconductors in large numbers, the quantum mechanical aspects of the material influence the formation of a plasma.

Carriers deposited in various conduction band minima will possess different dynamic characteristics than other carriers in other minima. Characteristics could vary by substantial amounts in terms of carrier energy and effective mass. These differences could allow plasmas to form against a background of other mobile carriers that do not share the same energy and effective mass.

This type of plasma would be highly dependent on the form and level of injection and the material's specific band structure.

3.5 NONEQUILIBRIUM PLASMAS

Situations occur in semiconductor materials where large quantities of charge can be injected or created via avalanche breakdown. This charge is self compensating (equal numbers of electrons and holes are created) and do not require compensation by immobile charge centers. This type of plasma is often strongly ionized (due to high electric fields) and easily populates the upper conduction band minima.

The four types of solid state plasmas outlined in this section would also possess different forms of plasma instabilities. The initially formed plasmas would be stable, but heating, geometry and changes in external electric fields and currents would force the plasma into a nonequilibrium state.

The simplest form of instability that would occur is similar to the plasma pinch effect initiated by the self-induced magnetic field of the carriers.

4.0 EQUILIBRIUM AND INSTABILITIES IN PLASMAS

Solid state plasmas differ from gaseous discharge plasmas in many aspects. In a simplistic sense, they represent extremes of the definition of plasma. Differences in carrier temperature and carrier density can be very large when comparing thermonuclear or stellar plasmas to solid state plasmas. Yet, all plasmas share the concepts of equilibrium and stability due to the processes of external interaction and confinement.

Since the semiconductor material is the confining bottle for a solid state plasma, problems of space-charge buildup, varying current flow, high electric fields, and nonlinear carrier dynamics must be faced. These aspects directly affect the plasma's thermodynamic equilibrium.

If the plasma is in the thermodynamic equilibrium with its surroundings, it is in a state of highest entropy, by definition. With the free energy available at a minimum, the plasma remains stable unless energy is provided externally to excite plasma waves (increase the available free energy). In a semiconductor, this additional free energy can come from a number of sources, but is limited in general to heating and external current sources. Plasma waves use extra free energy, at the expense of the plasma carriers, to rapidly grow and dominate plasma behavior. In reaction, the plasma assumes motion to decrease the available free energy and drive the plasma back toward thermodynamic equilibrium. This action is known as an instability.

Instabilities are classified under four categories depending on the driving force (or free energy) initiating the instability. These categories follow from basic instability phenomena found in gaseous discharge plasmas.

4.1 STREAMING INSTABILITIES

When a current is driven through a plasma, various species of carriers can take on different drift velocities with respect to each other. Plasma waves can grow by interacting with and stealing energy at the expense of the carriers' drift velocity resulting in Landau damping.

4.2 RAYLEIGH-TAYLOR INSTABILITIES

This type of instability comes from forming a nonuniform plasma that is driven from equilibrium by thermal or diffusive forces. A common example in solid state plasmas is the Gunn effect.

4.3 KINEMATIC INSTABILITIES

When the velocity distribution of carriers in a plasma are not Maxwellian, anisotropies can develop in plasma growth oscillation rates. For example, the perturbation of a plasma changes some of the plasma's potential energy into kinetic energy of motion.

4.4 UNIVERSAL INSTABILITIES

These instabilities occur due to the way a plasma is confined. If a solid state plasma expanded very rapidly and was physically confined by the material, instabilities would occur due to the rapid increase in free energy available. This type of instability may be difficult to observe because of the predominance of the other three types of instability.

These instabilities normally serve to dampen oscillations in a plasma, but the normal driving forces (free energy sources) in semiconductors act in a nonlinear fashion forcing oscillation growth. To control these instabilities, extraordinary precautions must be taken to control a semiconductor's nonlinear dynamics. This often includes a liquid nitrogen bath, quasi-steady state electric field application, and application of an external confining magnetic field.

Without precautions, a solid state plasma can rapidly move away from thermal equilibrium with the lattice with the ensuing instabilities forcing material damage from thermal shock.

5.0 DEVICE AND MATERIAL FAILURE

The postulation of the formation of solid state plasma in semiconductors caused by an overstress provides an additional clue to determining semiconductor failure. Since ionized solid state plasmas move away from thermodynamic equilibrium under normal device operation, the determination of that departure point is very important.

Previous work in the area of device failure attempted to model failure in a very simplistic fashion. Most models chose to relate thermal heating of the device to the input power via a simple empirical relation. These models could identify gross trends in device failure versus input pulse length, but sacrificed the accuracy of individual device failure levels in favor of ensemble trends. Attempts to relate this information to more detailed device physics has been, to date, unsuccessful.

Logically, this train of events leads researchers in device failure to examine the only area of research left: The detailed physics of device failure.

Second breakdown has been the traditional indicator of ensuing device failure for many years. The phenomena associated with second breakdown have also been well documented over this same time period. The evidence, detailed in many reports, points to the formation of a fine structure in the transport dynamics of the materials, that is unprecedented in ordinary knowledge of carrier transport. Simply stated, the isotropic current before second breakdown suddenly collapses into a high current density channel which grows and destroys the material by thermal shock.

The current-voltage characteristics displayed as second breakdown occurs are very similar to curves studied for the transition of single carrier to double carrier injection. Thus, it becomes apparent that a strong inference can be made connecting second breakdown to solid state plasma formation. In particular, it appears the common characteristic of current filament formation is similar to the strongly ionized plasma instability known as the Bennett pinch. This instability is quickly followed by rapid heating (also a consequence of the Bennett pinch) that could easily melt a semiconductor.

Other forms of instability can develop (as noted in the section of instabilities), but these are limited primarily to specific cases of device architecture, overstress characteristics and ambient conditions. The simplest connection, and possibly most insightful example of the relationship between second breakdown and device failure, is the examination of the solid state plasma under a Bennett pinch. This example will be used to show that the key to understanding device failure and second breakdown is intimately connected to the stability and characteristics of the solid state plasma.

6.0 FILAMENTATION DUE TO PINCH

6.1 THE BENNETT PINCH

Since the primary phenomenon associated with second breakdown is the formation of a current filament, a theory of second breakdown incorporating the solid state plasma must explain this phenomenon.

In plasma physics, the formation of a filament from an otherwise isotropic plasma is called the Bennett Pinch (Ref. 9). Basically, the flow of current carried in the plasma driven by an external electric field results in the formation of a self-magnetic field. The resulting interaction of E and B through the Lorentz equation produces a radial force on adjoining plasma tubes causing contraction (Fig. 1).

Under equilibrium conditions, the plasma carriers attain an isotropic temperature in a time long compared to changes in the pinch radius. When this is not true, a dynamic pinch must be used to model the effects.

6.2 THE EQUILIBRIUM PINCH

The equilibrium pinch starts with the general fluid equation of motion from kinetic theory.

$$m n \left(\frac{\partial \bar{U}}{\partial t} + (\bar{U} \cdot \nabla) \bar{U} \right) = q n (\bar{E} + \bar{U} \times \bar{B}) - \nabla \cdot \bar{P} + \bar{P}_{ir} \quad (9)$$

where

- m = mass of carrier
- n = number of carriers
- \bar{U} = velocity
- q = charge
- \bar{E} = electric field
- \bar{B} = magnetic field
- \bar{P} = pressure
- \bar{P}_{ir} = carrier collision factor

Under equilibrium

$$\left(\frac{d}{dt} \right) \bar{U} = \left(\frac{\partial}{\partial t} \right) \bar{U} + (\bar{U} \cdot \nabla) \bar{U} = 0 \quad (10)$$

so that

$$0 = q n (\bar{E} + \bar{U} \times \bar{B}) - \nabla \cdot \bar{P} + \bar{P}_{ir} \quad (11)$$

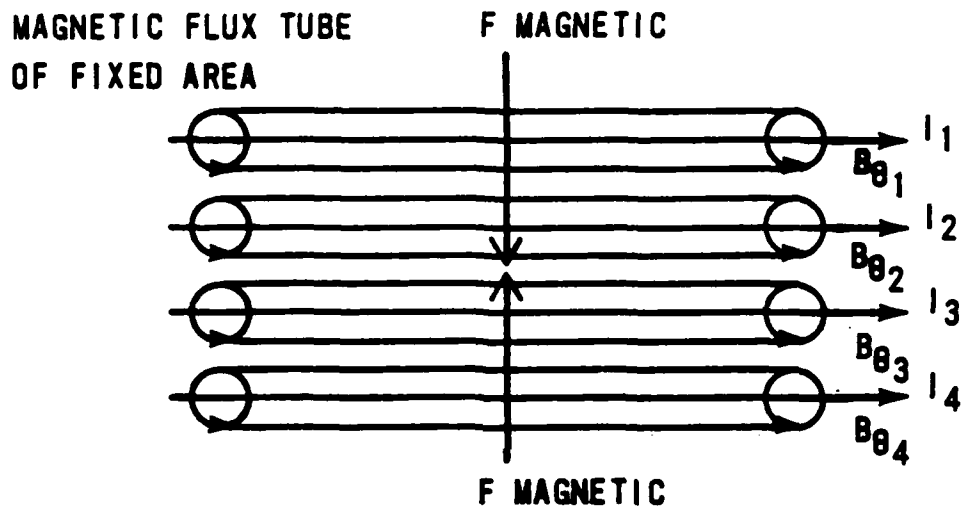


Figure 1. Once a sizable current is established the $J \times B$ force will cause an attraction of flux tubes - and a pinching of current lines.

Linearizing $\bar{P}_{i\alpha}$ in one direction so that

$$\nabla \cdot \bar{P} = \nabla P$$

results in

$$0 = qn(\bar{E} + \bar{V}_z \bar{B}) - \nabla P + \bar{P}_{i\alpha} \quad (12)$$

Writing Equations 11 and 12 out for electrons and holes

$$0 = -\nabla P_e - N_e e(\bar{E} + \bar{v}_{ez} \bar{B}) + \bar{P}_{eh} \quad (13)$$

$$0 = -\nabla P_h - N_h e(\bar{E} + \bar{v}_{hz} \bar{B}) + \bar{P}_{hr} \quad (14)$$

$$J = N_e e \bar{v}_e + N_h e \bar{v}_h \quad (15)$$

and

$$\bar{P}_{eh} = -\bar{P}_{he} \quad (16)$$

and adding Equations 13 and 14 gives

$$\nabla \bar{P} = J_z \bar{B} \quad (17)$$

For a cylindrical plasma column, the change of pressure with radius is

$$\frac{dP(r)}{dr} = -J_z(r) B_\theta(r) \quad (18)$$

as shown in Fig. 2.

Since the situation is symmetric, concern is primarily with one direction for current flow, so that

$$I_z(r) = \int_0^r J_z(r') 2\pi r' dr' \quad (19)$$

Placing Equation 20

$$B_\theta(r) = \frac{\mu_0 I_z(r)}{2\pi r} \quad (20)$$

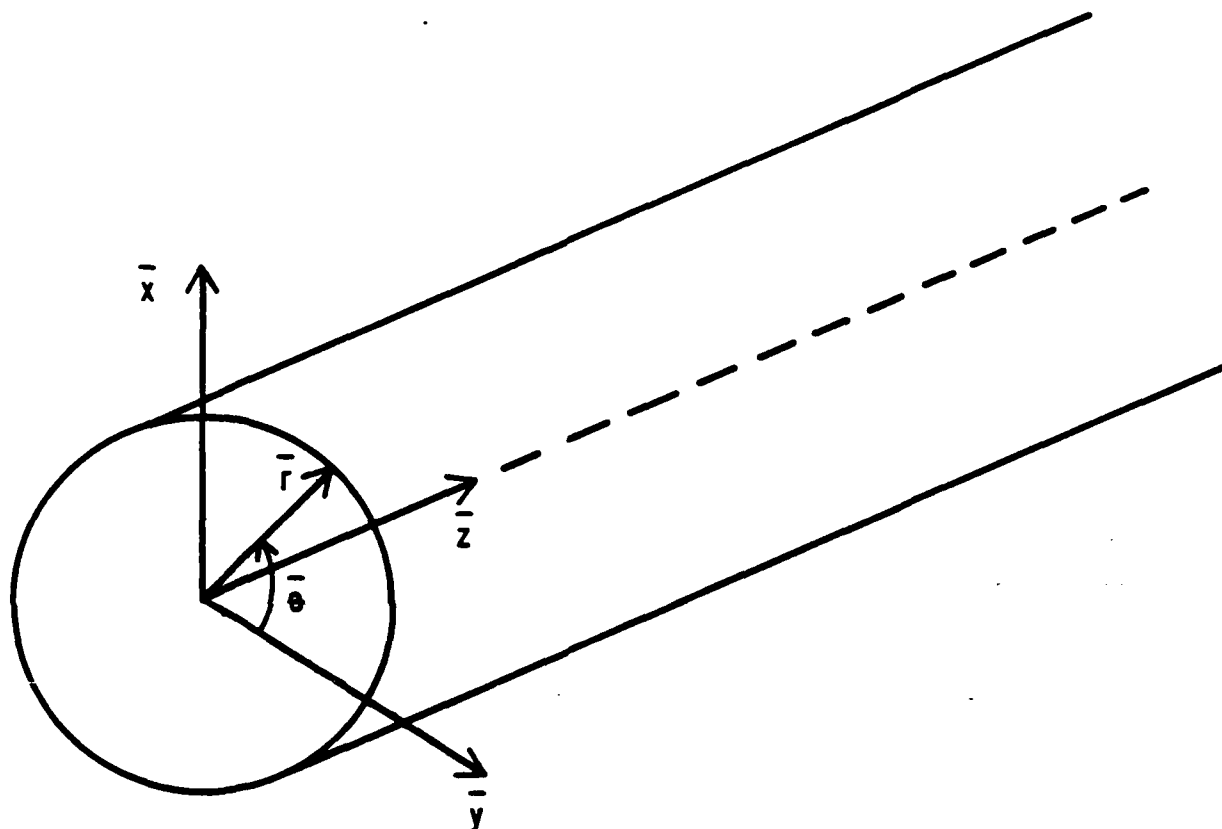


Figure 2. Cylindrical coordinate system applied to a plasma column under consideration. The plasma is assumed to be infinitely long so end effects can be ignored.

into Equation 18 results in

$$4\pi^2 r^2 \frac{dP(r)}{dr} = -\mu_0 I_z(r) \frac{d}{dr} I_z(r) = -\frac{d}{dr} \left(\frac{\mu_0 I_z^2(r)}{2} \right) \quad (21)$$

Integrating both sides from $r = 0$ to R , and integrating by parts on the left-hand side (LHS) of Equation 21 results in

$$\int_0^R 4\pi^2 r^2 P(r) dr = - \int_0^R \frac{\mu_0 I_z^2(r)}{2} dr = - \frac{\mu_0 I_z^2(R)}{2} \quad (22)$$

using $I_z(0) = 0$, next gives

$$4\pi^2 r^2 P(r) \Big|_0^R - 4\pi \int_0^R 2\pi r P(r) dr = - \frac{\mu_0 I_z^2(R)}{2} \quad (23)$$

$P(r)$ is nonzero and finite for $0 \leq r \leq R$ and zero for $R \leq r \leq \infty$. the LHS of Equation 23 is zero and $P(r) = N(r)k(T_c + T_h)$ gives

$$- 4\pi \int_0^R 2\pi r k(T_c + T_h) N(r) dr = - \frac{\mu_0 I_z^2(R)}{2} \quad (24)$$

let $N_t = \int_0^R N(r) 2\pi r dr$ be the number of carriers per unit length of the column, then

$$I_z^2(R) = \left(\frac{8\pi}{\mu_0} k(T_c + T_h) N_t \right) \quad (25)$$

is the critical current (in MKS) required to initiate pinch for a specific temperature and carrier number. Equation 25 is known as the Bennett relation. For a unit bar of silicon with a doping level of 1×10^{14} carriers/cm³ I_c is about 0.87 mA. Of further interest is the distribution of $P(r)$, $J_z(r)$, and $B_\theta(r)$ from the Bennett relation.

To investigate how Equation 18 changes, the plasma are assumed to be ideal; that is, they possess an infinite conductivity. Thus, the current is restricted to the surface of the plasma cylinder. From the law of magnetostatics $\nabla \times B(r) = \mu_0 J(v)$. so

$$J_z(r) = \frac{1}{\mu_0 r} \frac{d}{dr} \{r B_\theta(r)\} = \frac{1}{\mu_0} \frac{d}{dr} B_\theta(r) + \frac{B_\theta(r)}{\mu_0 r} \quad (26)$$

which placed in Equation 18 yields

$$\begin{aligned} \frac{d}{dr}P(r) &= -\frac{B_\theta(r)}{\mu_0} \frac{d}{dr}B_\theta(r) - \frac{B_\theta^2(r)}{\mu_0 r} \\ &= \frac{1}{2\mu_0 r^2} \frac{d}{dr}\{r^2 B_\theta^2(r)\} \end{aligned} \quad (27)$$

Integration from zero to r arrives at

$$p(r) = p(0) - \frac{1}{2\mu_0} \int_0^r \frac{1}{r^2} \frac{d}{dr}\{r^2 B_\theta^2(r)\} dr \quad (28)$$

Since $P(r) = 0$ we get

$$P(0) = \frac{1}{2\mu_0} \int_0^R \frac{1}{r^2} \frac{d}{dr}\{r^2 B_\theta^2(r)\} dr \quad (29)$$

which when replaced in Equation 28 yields

$$P(R) = \frac{1}{2\mu_0} \int_r^R \frac{1}{r^2} \frac{d}{dr}\{r^2 B_\theta^2(r)\} dr \quad (30)$$

with

$$I_z(r) = \int_0^r J_z(r) 2\pi r dr \quad \text{and} \quad B_\theta(r) = \frac{\mu_0 I_z(r)}{2\pi r} \quad (31)$$

$P(r)$ can be examined if $J_z(r)$ is known. By assuming that $J_z(r)$ is concentrated at the surface ($r = R$), then $B_\theta(r)$ exists outside the column and $P(r) = P(0)$, so pressure is constant (see Fig. 3).

Also, since

$$\langle P(r) \rangle = \frac{1}{\pi R^2} \int_0^R 2\pi r P(r) dr \quad (32)$$

$$\langle P(r) \rangle = \frac{1}{R^2} \left[r^2 P(r) \Big|_0^R - \int_0^R r^2 \frac{d}{dr} P(r) dr \right] \quad (33)$$

combined with Equation 17, the first term on the right-hand side (RHS) is zero. Thus,

$$\langle P(r) \rangle = \frac{B_\theta^2(R)}{2\mu_0} \quad (34)$$

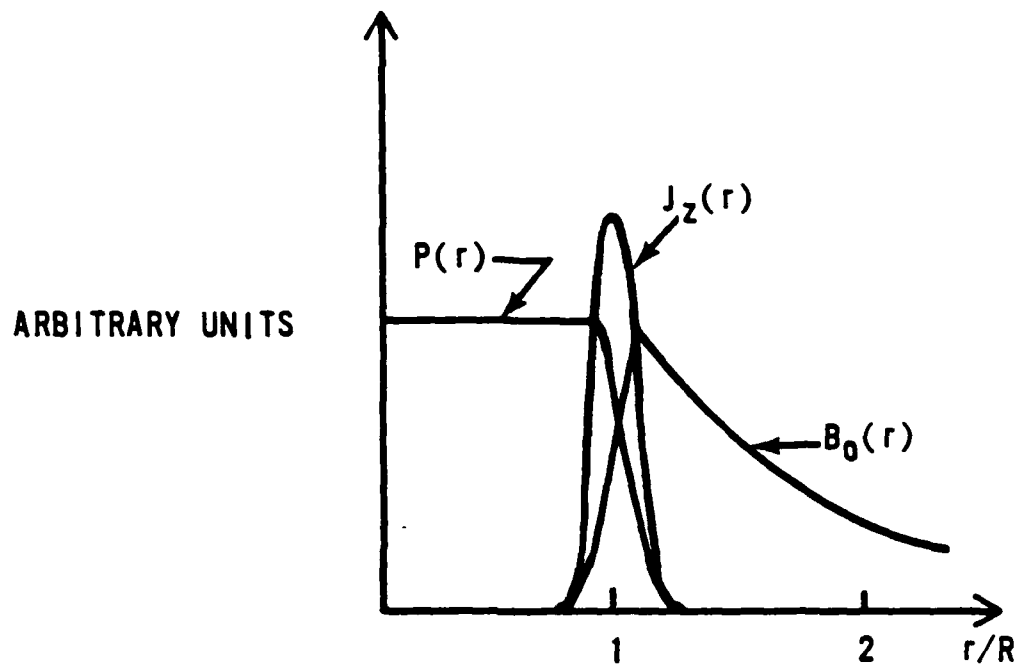


Figure 3. Distributions for $P(r)$, $J_z(r)$, and $B(r)$ for a current sheath at the edge of the plasma column.

The average pressure inside the column (which is constant for this case) is balanced by the magnetic pressure at the column surface.

If a solid state plasma exhibited an infinite conductivity, the column would possess ballistic transport qualities. Although it is possible to attain ballistic trajectories in a semiconductor, the necessary conditions are quite severe. Thus, ballistic transport is unlikely to dominate current transport processes under normal conditions. It is possible that the carrier concentration, carrier mobility or transit times could reach levels where the conductivity was quite high compared to other portions of the device (resembling a strongly ionized plasma). Current could then be monotonically increasing with distance from the center of the cylinder (this has been postulated in Ref. 10 and the above derivation seems to support the idea).

Another possible distribution is $J_z(r) = \text{constant}$ across the entire cylinder and zero at $r = R$. In this case,

$$B_\theta(r) = \frac{\mu_0 J r}{\pi R^2} \quad (35)$$

Substitution of this value of $B_\theta(r)$ into Equation 30 generates

$$\begin{aligned} P(R) &= \frac{1}{2\mu_0} \int_r^R \frac{1}{r^2} \frac{d}{dr} \left(r^2 \frac{\mu_0^2 J^2 r^2}{\pi^2 R^4} \right) dr \\ P(R) &= \frac{\mu_0 J^2}{\pi^2 R^4} \int_r^R \frac{d}{dr} (r^4) dr \\ P(R) &= \frac{\mu_0 J^2}{\pi^2 R^2} \left(1 - \frac{r^2}{R^2} \right) \end{aligned} \quad (36)$$

a parabolic dependence of pressure on radius (Fig. 4). This example would be found for a weakly ionized plasma.

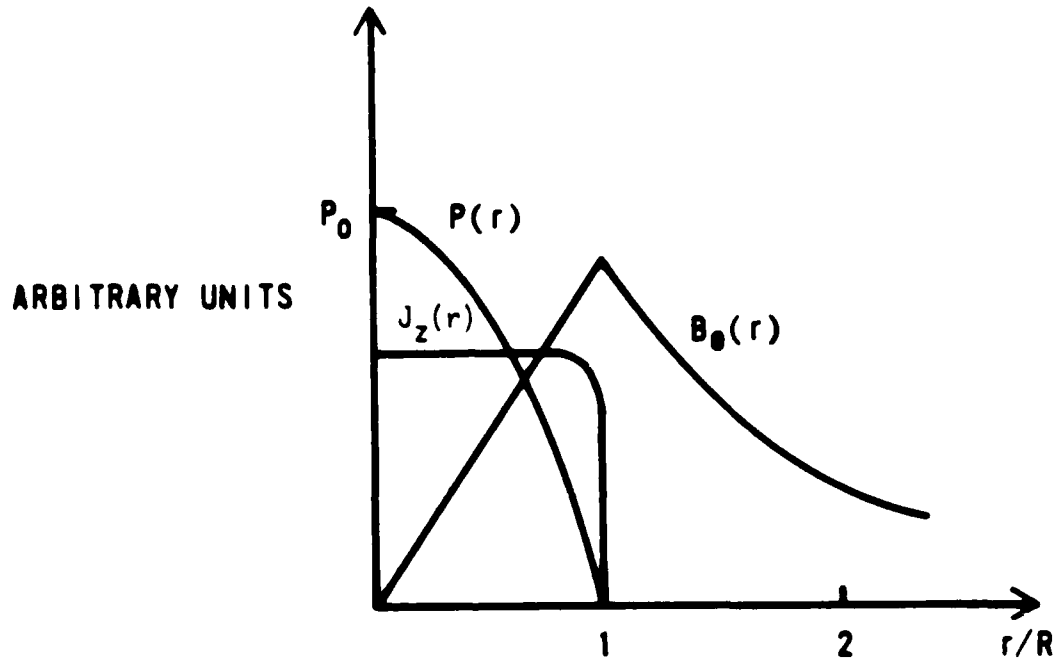


Figure 4. Distribution for $P(r)$, $J_z(r)$, and $B_0(r)$ for a constant density across the plasma column.

To get a better understanding of $J(r)$'s possible distribution, refer to Bennett's original study (Ref. 9). In that study, Bennett found the distribution or $N(r)$ which relates to $J(r)$ via

$$J_s(r) = N(r)e^{(v_c + v_h)} \quad (37)$$

which relates to $P(r)$ and $B(r)$ by

$$\frac{dP(r)}{dr} = -J_s(r)B_0(r)$$

$$P(r) = N(r)k(T_c + T_h)$$

$$\frac{d}{dr}\{N(r)k(T_c + T_h)\} = -N(r)e^{(v_c + v_h)}B_0(r)$$

$$\frac{d}{dr}N(r) + \left\{\frac{e^{(v_c + v_h)}}{k(T_c + T_h)}\right\}N(r)B_0(r) = 0$$

Multiplying by $r/N(r)$ and taking the derivative, replacing with

$$\frac{d}{dr}\{rB_0(r) - N(r)e^{(v_c + v_h)}\} = \frac{1}{\mu_0 r} \frac{d}{dr}\{rB_0(r)\}$$

results in

$$\frac{d}{dr}\left\{\left(\frac{r}{N(r)}\right) \frac{d}{dr}N(r)\right\} + 8brN(r) = 0 \quad (38)$$

where

$$b = \frac{\mu_0 e^2 (v_c + v_h)^2}{8k(T_c + T_h)}$$

With the boundary conditions that $N(r)$ is symmetric about $r = 0$, and smoothly varying so that $\frac{d}{dr}N(r) = 0$ at $r = 0$, the solution is

$$N(r) = N_0[1 + bN_0r^2]^{-2} \quad (39)$$

where $N_0 = N(r)$ at $r = 0$. Equation 39 is called the Bennett distribution (Fig. 5).

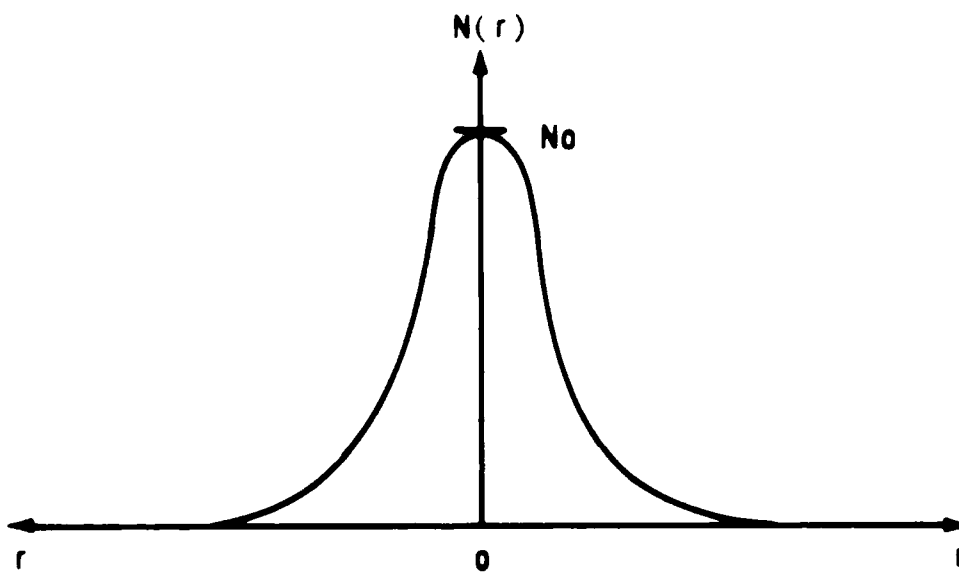


Figure 5. Graph of the Bennett Distribution.

For a solid state material, N_0 can be related to the intrinsic and injected carrier concentration. N_1 will have a temperature dominated factor and an injection process related field factor.

To relate $N(r)$ back to N_1 of Equation 25,

$$N_i(R) = \int_0^R 2\pi r N(r) dr = \int_0^R 2\pi r N_1 (1 - N_1 b r^2)^{-2} dr$$

$$N_i(R) = N_1 \pi R^2 (1 - N_1 b R^2)^{-1} \quad (40)$$

But the plasma extends to $r = \infty$, so

$$N_i(R) = \frac{\pi}{b}$$

If α is defined as a fraction of $N_1(\infty)$ in a finite cylinder of radius, then

$$N_i(R) = \alpha N_i(\infty) = \alpha \frac{\pi}{b}$$

substituting what into Equation 40 results in

$$\sqrt{N_0 b} R = \left(\frac{\alpha}{1 - \alpha} \right)^{1/2}$$

If $\alpha = 0.9$, or 90 percent of the carriers are within the cylinder of concern, the last equation becomes

$$\sqrt{N_0 b} R = 3 \quad (41)$$

defining the relation of R to our problem in a simple manner.

The Bennett distribution can now be used to derive the applicable $P(r)$ and $B(r)$ values

$$J_z(r) = N(r)e|v_e + v_h| = N_0(1 + bN_0r^2)^{-2}e|v_e + v_h|$$

$$I_z(r) = \int_r^R 2\pi r N_0(1 + bN_0r^2)^{-2}e|v_e + v_h| dr = 2\pi N_0e|v_e + v_h| \int_r^R r(1 + bN_0r^2)^{-2} dr$$

$$I_z(r) = 2\pi N_0e|v_e + v_h| \left(\frac{-1}{2bN_0} \frac{1}{(1 + bN_0R^2)} + \frac{1}{2bN_0(1 + bN_0r^2)} \right)$$

$$I_z(r) = N_0\pi e|v_e + v_h| \left(\frac{R^2 - r^2}{(1 + bN_0r^2)(1 + bN_0R^2)} \right) \quad (42)$$

for $B_0(r)$

$$B_0(r) = \frac{\mu_0 I_z(r)}{2\pi r}$$

$$B_0(r) = \frac{\mu_0 e|v_e + v_h|}{20b} \left(\frac{9 - N_0br^2}{(r + N_0br^2)} \right)$$

and for $P(r)$

$$\frac{dP(r)}{dr} = -J_z(r)B_0(r)$$

Substitution of $B_0(r)$ above into $P(r)$ is extremely difficult to solve and yields the following relation after the use of integral tables:

$$\begin{aligned} P(r) = C \left[\frac{9}{2} \left(\frac{1}{R(1 + N_0bR^2)} + \frac{1}{R(1 + N_0bR^2)^2} + \log \frac{R^2}{(1 + N_0bR^2)} \right) \right. \\ \left. - \frac{9}{2} \left(\frac{1}{r(1 + N_0br^2)} + \frac{1}{r(1 + N_0br^2)^2} + \log \frac{r^2}{(1 + N_0br^2)} \right) \right. \\ \left. + \left(\frac{N_0b}{4N_0b(1 + N_0bR^2)^2} - \frac{N_0b}{4N_0b(1 + N_0br^2)^2} \right) \right] \quad (43) \end{aligned}$$

where

$$C = \frac{-N_0e^2\mu_0|v_e + v_h|^2}{20b}$$

The form of $N(r)$ in this example possesses attributes of the strongly and weakly ionized plasma. Near the center of the column, the plasma is strongly

ionized and slackens in activity as r increases in distance from the center.

6.3 THE DYNAMIC PINCH

If the equilibrium condition for the equilibrium pinch cannot be met, the dynamic pinch must be applied.

By starting with a known input current

$$B_{\theta}(r) = \frac{\mu_0 I(r)}{2\pi r}$$

and

$$P_m(r) = \frac{B_{\theta}^2(r)}{2\mu_0} = N(r, t)k(T_e(r, t) + T_h(r, t))$$

can be used to find the inward force on a collapsing current sheath. As the sheath collapses inward, it collects plasma in front of it. Hence, this model is called the snowplow model. The collapsing force is equated to the plasma's rate of change of momentum to arrive at the equation of motion.

In a manner similar to a mechanical system, the snowplow model shows (Ref. 11) that a shock wave initiated by the pinch reflects off the axis and back to the pinch front resulting in an oscillation.

Instead of displaying a constant pinch radius, a dynamic pinch plasma oscillates around the equilibrium radius established by the input current and plasma parameters. This effect has been called bounce. If the input current oscillates, it is possible to initiate an instability that will continue throughout current application (see experimental evidence in Ref. 10). Dynamic pinch problems are difficult to verify when applied to the solid state plasma. Use of Monte Carlo modeling should begin to eliminate problems in modeling the dynamic pinch.

7.0 GROWTH INSTABILITIES OF THE EQUILIBRIUM SOLID STATE PLASMA

As mentioned in the section on equilibrium and instabilities, four different categories of instabilities are possible: Streaming instabilities, Rayleigh-Taylor instabilities, Kinematic instabilities and Universal instabilities. These four categories can be placed under the general categories of configuration space instabilities and velocity space instabilities.

These last two categories are useful in explaining the type of instabilities formed in semiconductor plasma formation from electrical or optical excitation.

Under electrical excitation the transition from single- to double-carrier injection under low fields is the main impetus to form a weakly ionized plasma. Avalanche breakdown, high electric fields, or high temperatures usually form strongly ionized plasmas. The differences between these two conditions also determine the type of instability that can occur.

7.1 SAUSAGE INSTABILITY

If an otherwise cylindrical plasma is perturbed by an external force causing a spatial variation of the plasma, a new equilibrium position will be reached. But, in moving to a new equilibrium position, free energy may be released resulting in an instability.

As Fig. 6 shows, bulges can form in the plasma as stationary or moving waves. The increased current density in pinched portions of the plasma will create an increased magnetic field around the pinch. In areas where the plasma has extended, the decreased current density lowers the magnetic field strength allowing plasma pressure to expand outward. These mechanisms can work in concert to actually pinch the column off. Externally, rapid oscillations in current are measured as this instability occurs.

In a semiconductor diode (PN or PIN), this type of instability readily occurs due to the depletion layer configuration. Since current streams out of the plasma column ends, and kinetic and magnetic pressures are highest at the center of the column length, the sausage instability forms upon the plasma reaching the depletion edge (Fig. 7).

Similar situations can occur for PIN diodes, and transistors for collector-emitter, collector-base and emitter-base plasma formation. Avalanche breakdown

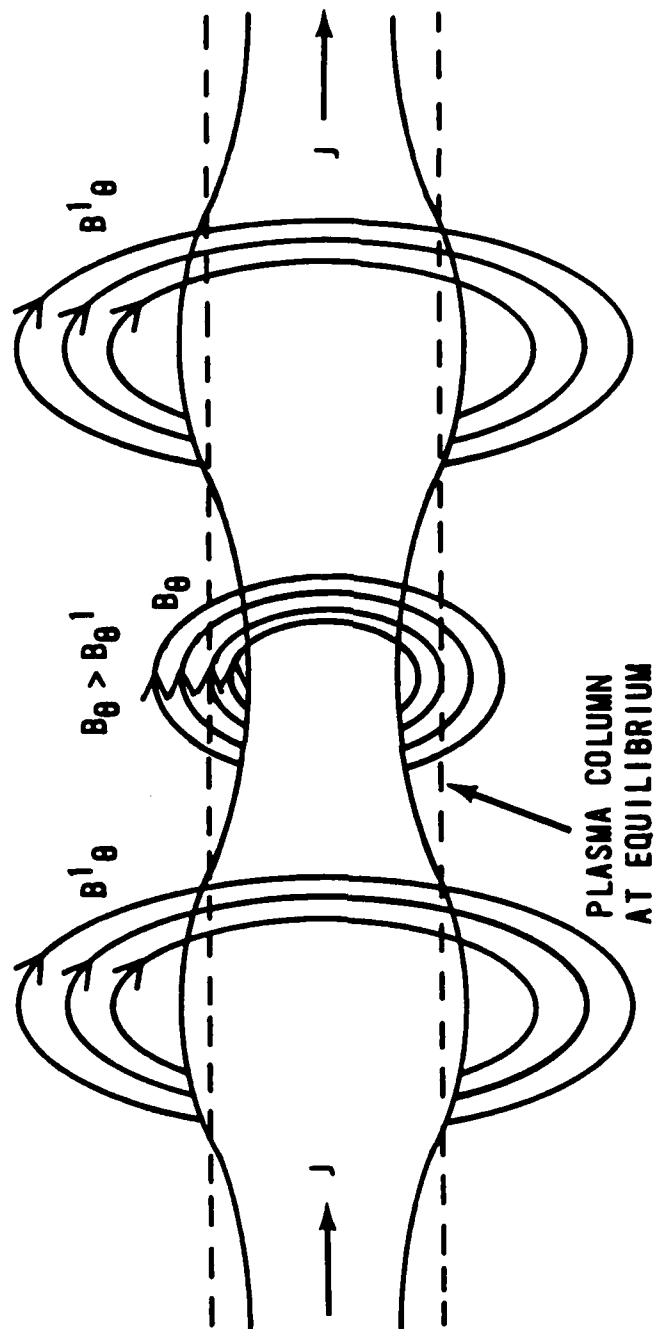


Figure 6. Illustration of a plasma column undergoing the sausage instability. As the instability grows, B_θ will almost pinch off current at troughs, and kinetic pressure will elongate crests at B'_θ . Current measured during this instability will be sinusoidal in nature.

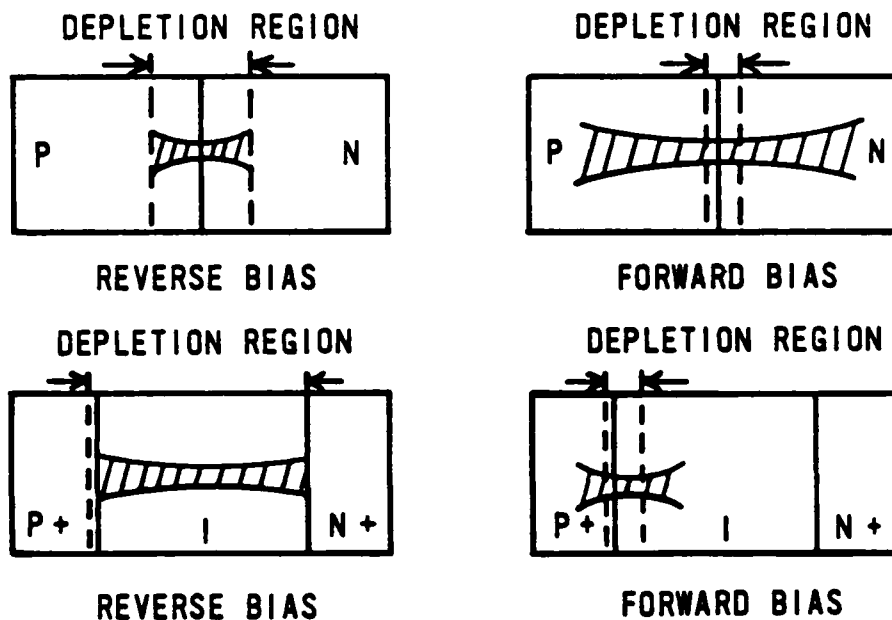


Figure 7. Depiction of possible areas of plasma formation in PN and PIN diodes. The shaded areas show a plasma column with fluted ends. The shape is indicative of a sausage instability which may occur upon pinch due to the devices geometry. Most experiments that study plasma pinch in semiconductors see oscillations simultaneously with plasma formation.

in the midst of plasma formation will cause a perturbation in the column that will resemble the sausage instability.

If avalanche has already occurred, initiating plasma formation, extensive heating near the pinch center could cause a sausage instability. This event could also be explained as the beginning of a thermal pinch, to be described later in the report.

7.2 KINK INSTABILITY

If the plasma column is disturbed by a relatively large perturbation caused by device construction, the kink instability occurs.

As Fig. 8 illustrates, the magnetic field lines are more concentrated in Region 1 than in Region 2. Thus, the magnetic pressure is greater in Region 1 than in Region 2. A kink started in this manner uses this feedback mechanism to easily continue the initial perturbation.

Because of transistor construction using mesa architecture (as shown in Fig. 9), a kink instability due to base current flow can easily form.

If a surface is near the direction of instability, surface recombination could aid instability growth. In a transistor, such action would appear to increase the base resistance to current flow and debias the emitter under collector-emitter breakdown in the common-emitter mode.

A second cause for the kink instability is plasma formation in depletion regions that curved perpendicularly to current flow.

7.3 STREAMING INSTABILITIES

It is well known from classical mechanics that two dynamic systems interact most effectively if the system velocities or frequency of oscillations are about the same.

In a semiconductor, the mass difference between holes and electrons produces two separate dynamic systems for the semiconductor plasma. The plasma, as a whole, oscillates at a frequency (separate from the electron and hole plasma frequencies) in such a way that its phase velocity is normally higher than the carriers' thermal velocity by a large magnitude, thereby preventing any exchange of energy.

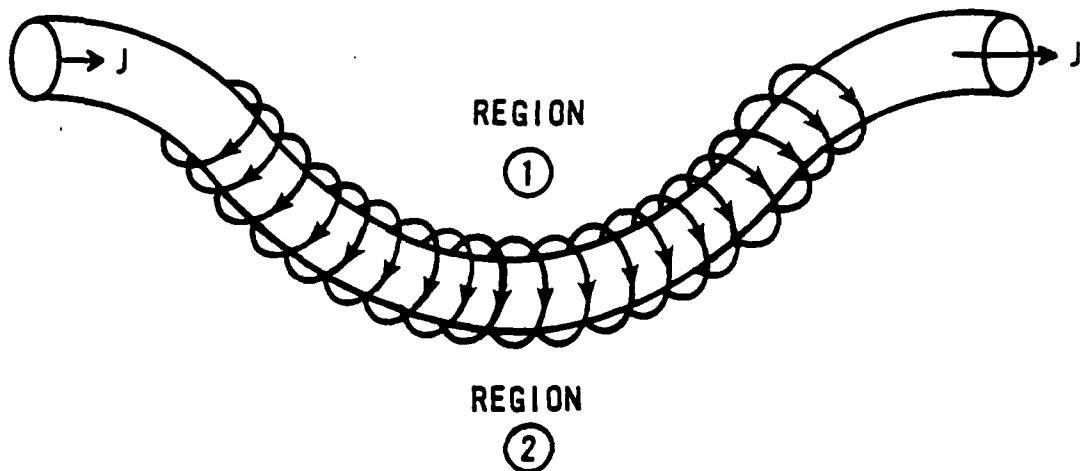


Figure 8. Kink instability. The perturbed column creates a curvature that increases the magnetic pressure in region (1) at the expense of lessening it in region (2). The kinetic pressure responds by exerting greater pressure towards region (2). The feedback forces the kink to continue to grow in the direction of region (2).

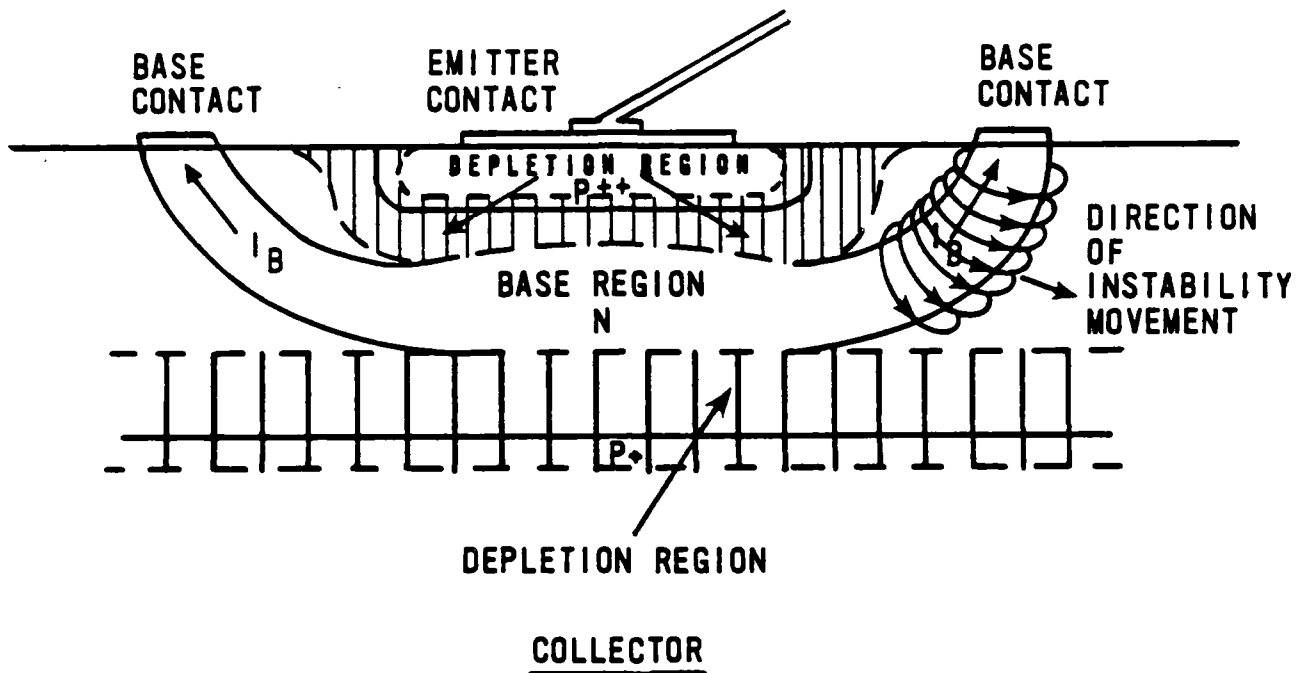


Figure 9. A mesa P-N-P transistor in the common-emitter mode in cut-off. As current is withdrawn from the base, plasmas may form and current crowding may instigate kink instabilities leading to further current crowding.

As carriers heat up, their velocities approach the plasma's phase velocity. As their velocities surpass the phase velocity, the plasma oscillations gain energy from their carriers' velocities, slowing some carriers down and speeding others up. This process changes the normal one-hump Maxwellian velocity curve to a two-hump curve. The plasma oscillations grow in magnitude from the external energy source resulting in the two stream instability (Ref. 12, Fig. 10).

The growing plasma oscillations begin to transfer energy back to the lattice via optical or acoustic phonon excitation, heating the lattice till it melts and enters the thermal pinch phase.

The two-stream instability can occur via excitation of the plasma by heating or an increasing electric field. It can also occur as a consequence of the quantum mechanical aspects of a semiconductor material.

The formula relating the carrier velocity to plasma phase velocity for occurrence of the two-stream instability was discerned by Pines and Schrieffer (Ref. 13) as the following in the long wavelength limit.

$$\text{The electron thermal velocity} = v_e = \left(\frac{2kT_e e}{m_e} \right)^{\frac{1}{2}}$$

If $T_e = T_h$, then the threshold is

$$v_D = 0.93v_e \left(1 + \left(\frac{m_e}{m_h} \right)^{\frac{1}{2}} \right)$$

when the relative drift velocity, V , is equal to the electron thermal velocity.

However, m_e and m_h are dependent on crystal orientation and carrier excitation level. As carriers gain enough energy to enter the conduction band, they eventually enter other minima that reduce the carrier's effective mass; thus, increasing the value of v_e and v_D , which interact with higher energy phonons in a strongly coherent manner.

This type of plasma formation would occur for very rapid excitation of a semiconductor by an optical or electric field, and should be dependent on the crystal orientation and band structure. The occurrence of this instability would rapidly degrade to a thermal pinch under room temperature conditions. Actual measurement of this instability has been accomplished at low temperatures for n-type InSb (Ref. 14).

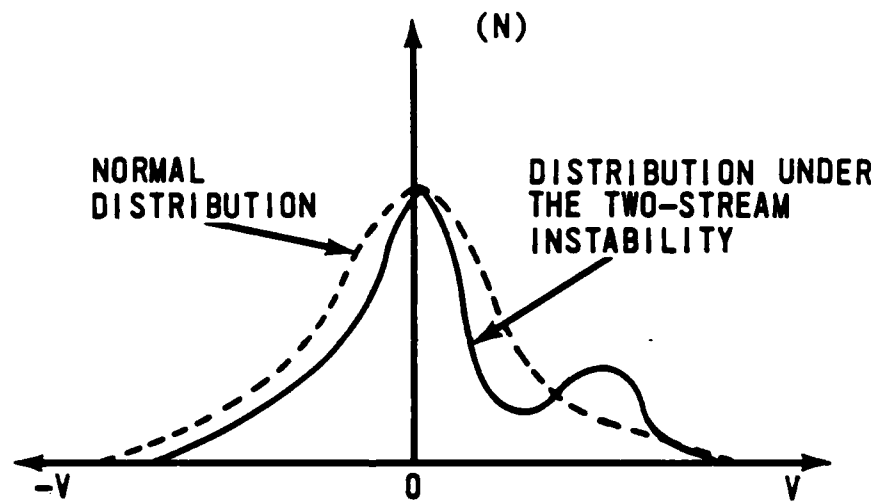


Figure 10. Unstable Maxwellian distribution. The unstable distribution is produced by the two-stream instability.

8.0 THERMAL PINCH

At the high temperatures produced by semiconductor plasmas under extreme conditions, a type of instability occurs that is the result of a magneto-thermal pinch transitioning to a pinch dominated by thermodynamic driving forces.

This type of pinch has been labeled the thermal pinch (Ref. 15) to distinguish it from the previous discussion of a magneto-thermal pinch.

When heating in the core of a magneto-thermal pinch reaches levels where the intrinsic carrier concentration rises rapidly to create a degenerate plasma, the kinetic pressure quickly overcomes the magnetic pressure. The material begins to change phase from a solid to a liquid and expands rapidly to engulf the available region. This type of pinch can literally explode out the ends of the semiconductor being pulsed and totally dominates the prefailure electrical characteristics.

Proof for this type of pinch was discovered by Betsy Ancker-Johnson and James Drummond in References 10 and 15. Their experiments with InSb actually formed hollow melt channels in the specimens examined. Additional measurements showed a distinct trend for pinch channel radius found via Bennett's temperature (using the magneto-thermal pinch) to move toward a channel radius dictated by the semiconductor melting temperature (or thermal pinch) as shown in Fig. 11.

Since the thermal pinch literally moves through a material in a manner similar to electromigration, its velocity of propagation is highly dependent on the material configuration and thermodynamic properties (heat of fusion, coefficient of expansion, available energy to do work in the plasma, and geometry).

The dependence of the thermal pinch on so many micro- and macroscopic variables makes modeling of a thermal pinch in devices very difficult, and somewhat probabilistic.

This is the type of plasma formation that occurs in semiconductor devices pulsed to destruction. The character of the thermal plasma pinch would add a variable character that may explain the variation found in experimental studies (Ref. 1).

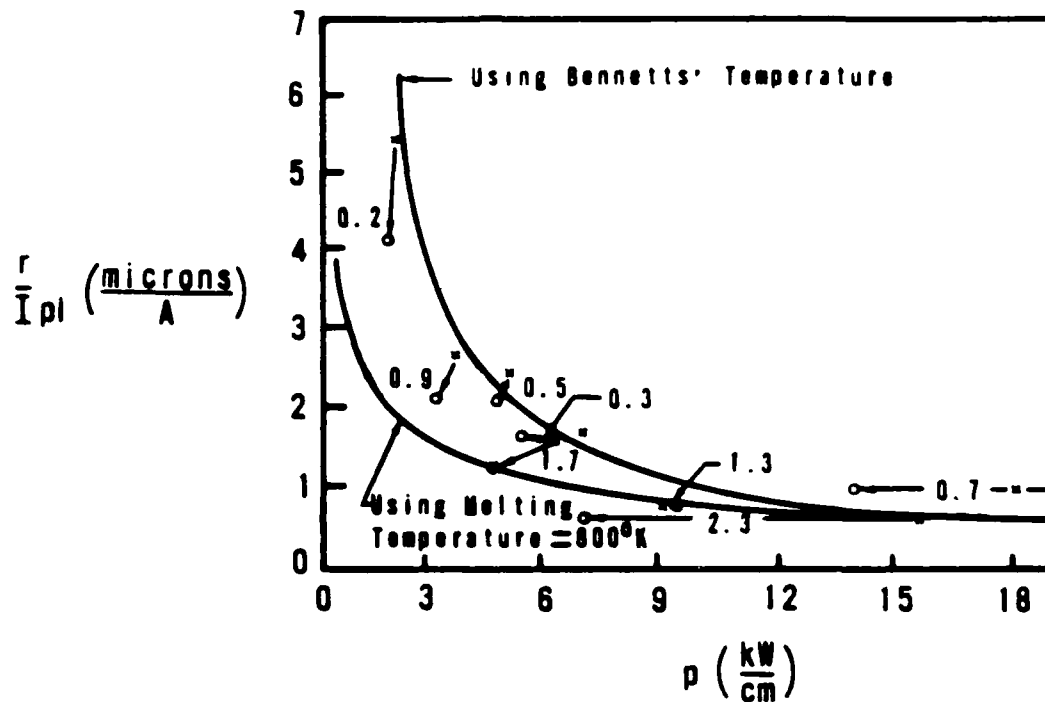


Figure 11. The pinch radius divided by the plasma current as a function of power input per unit length of plasma: Experimental data at the onset of pinching (x), at the end of the pulses (o). The upper curve is the result of magnetic theory and the lower, thermal pinch theory. The numbers associated with the arrows correspond to the net energy transferred to the pinch column in units of energy required to melt the column (Ref. 15).

Theoretical analysis of device failure based on thermal models would then be able to model some general trends, but would be totally inadequate to explain propagation of the thermal pinch or the initiating conditions prompted by the magneto-thermal pinch. These models do not simulate plasma effects or changing solid state parameters that affect the plasma.

In optical induced failure, the thermal pinch also represents an extreme of the pinch phenomena. Once thermal pinching occurs, the plasma would blossom outward actually melting the material. The model put forth by Ancker-Johnson et al in References 15 and 16 should provide a good starting point to determine the initial conditions surrounding optically induced failure in semiconductors.

The Monte Carlo program produced for this effort still must be modified to model the thermal pinch.

9.0 MONTE CARLO METHOD

Damage to semiconductor devices by intense electromagnetic pulses has been studied over many decades. However, understanding of damage mechanisms at the level of basic physical processes is still very incomplete. This is not surprising in view of the complexity, in terms of solid-state device physics, of the phenomena involved. With the intense fields that cause damage, basic analysis requires much more accurate energy band structure and carrier scattering rates than have been adequate heretofore even for most problems in high field transport. Moreover, damage occurs typically through a series of rather distinct stages. A complete theoretical treatment also involves modeling collective effects, such as space charge and carrier-carrier scattering, in order to describe the later stages. However, it can now be said that all of these difficulties are tractable. Spurred by its importance in microelectronics, progress in the numerical calculation of high-field transport effects has produced computational techniques for treating these necessary refinements (Refs. 17 and 18). It remains now to combine the various methods and apply the resulting computational power to the problem of device damage.

A damage mechanism, such as second breakdown (Ref. 19), occurs in a device when the electromagnetic field exceeds a threshold value. It evolves from an initial precipitative stage of carrier growth, through one or more stages where the effects of large current and charge densities are important, to a final phase of material breakdown. In general, space, as well as time dependence, enters (particularly in the later stages of plasma development) even for the case of damage in the homogeneous bulk.

Full understanding of a phenomenon requires its description at the microscopic level. Consider the mechanism by which negative differential mobility occurs in the bulk of certain semiconductors. This hot electron phenomenon is a transferred electron effect (Ref. 19). When the electric field exceeds some threshold value, electron scattering from the lowest valley to upper valleys of the conduction band becomes large enough to cause significant repopulation to the upper valleys. The (steady state) mobility thereafter decreases with increasing field. Once this basic description is known, one has a unifying theory whereby it is possible to predict the occurrence and

magnitude of the effect in various semiconductors from a knowledge of their band structure and scattering properties.

When an external electromagnetic field is applied to a conducting material, the most complete quasiclassical description of the resulting charge transport is given by the carrier distribution function $f(\bar{r}, \bar{p}, t)$. This specifies the statistical distribution of mobile charge carriers over phase (momentum \bar{p} plus coordinate \bar{r}) space. In the absence of both external fields and temperature gradients, the distribution function is everywhere independent of time and is that of thermal equilibrium, viz., a Fermi-Dirac distribution. Upon application of a field which is thereafter time independent dc or periodic of constant amplitude, the distribution rapidly attains a steady state form (possibly with spatial variation) that describes the steady-state charge transport resulting. In a truly transient situation, such as that of a damage mechanism, the distribution function will have temporal as well as possible spatial dependence as the carriers respond change in the field acting on them.

In the quasi-classical picture of charge transport, the mobile carriers are approximately independent particles. For crystalline materials, carriers occupy the stationary quantum Bloch states of the perfect ionic lattice. The free-electron-like Bloch states are each specified by a value of crystal-momentum vector \bar{p} , and the energy eigenvalue of a state is given by the applicable band structure function $E(\bar{p})$. The state of a carrier will change as the result of deviations from perfect crystal periodicity caused by phonons (lattice vibrations), impurities and imperfections, and by the presence of other carriers. The transition of a carrier state that occurs in an interaction with one of these perturbation sources is described as a scattering (or collision) event. A scattering event is governed by the laws of quantum mechanics. For each type of scattering process, there is a probabilistic scattering function $P_i(\bar{p}, c; \bar{p}', c')$, which is the transition probability per unit time for a carrier in state \bar{p} with the crystal in state c to scatter into the state \bar{p}' leaving the crystal in state c' .

In the thermal equilibrium, the carrier distribution gives detailed balance between any scattering event and its time-reversed event. The thermal motion of the carriers is completely chaotic with no net transport of charge or energy. Where no built-in field is present, the Bloch state of a carrier remains unchanged between collisions.

Charge transport occurs if an external field is applied. In free flight between two consecutive scatterings, a carrier moves solely under the force of the electromagnetic field acting on it and its momentum changes in accordance with the classical laws of motion. Each free flight is randomly interrupted when the carrier interacts with the lattice or with another carrier. Thus, the state of a carrier varies continuously through the Bloch states as it is accelerated by the field during a free flight. But the state changes abruptly and the change can be large in the scattering event that terminates the flight. The distribution function in this quasi-classical picture is governed by the Boltzman transport equation (BTE), which incorporates the effects on the distribution of the dynamical processes (carrier acceleration by the field and carrier collisions) and of spatial or temporal variations in the distribution. The departure of the distribution function from equilibrium with the lattice increases with the strength of the applied field. It is usually permissible to consider the phonon distribution as always thermalized.

The values of the distribution function at relatively fine-grained cells in phase space comprise a huge amount of information, often more than is desired. Physical quantities characterizing carrier motion, such as carrier energy $E(\bar{p})$ and velocity $\nabla_{\bar{p}} E(\bar{p})$, are functions of momentum. Significant parameters in charge transport are the average of such quantities over the distribution function throughout momentum space or in a certain region of momentum space (such as an energy valley). In most cases, the salient features of a phenomenon are revealed by the behavior of a relatively few transport parameters and by the coarse-grained dependence of the distribution function on some momentum component or on energy.

Detailed analysis of damage at the level of fundamental physical processes requires more powerful and complex computational methods than have previously been brought to bear on the problem. But numerical analysis of high-field (hot-carrier) behavior of semiconductor devices has now advanced to where such first-principles modeling can be applied to the extreme fields that cause damage. Once the roles of basic physical properties are properly understood for a particular mechanism, a reliable theoretical basis will be available for developing devices more resistant to damage from this cause. One can hope thereby to make optimum decisions on material selection, device

design, and circuit characteristics. An additional benefit will accrue in the area of device engineering. The simplified equations commonly used in device analysis and design can be made more accurate and confidence limits set for their application in the damage regime. The transport parameters appearing in these equations can be calculated with the help of detailed numerical methods and their predictions can be compared with the relatively exact calculations (Ref. 20).

9.1 NUMERICAL ANALYSIS OF SEMICONDUCTOR DEVICES

To properly understand and design today's electronic devices requires detailed modeling of the space- and time-dependent charge and current distributions at the operating potentials of interest. Numerical computations are generally resorted to (1) when the device equations do not admit analytic solutions because of complicated transient effects or spatial structures, (2) when device transport is nonlinear because of hot-carrier contributions, and (3) in computer-aided design of devices that require multidimensional structures for their operation.

The behavior of a solid state device whose dimensions are greater than one micron has conventionally been analyzed (particularly in the case of silicon) by means of the semiconductor equations. These equations are based on the classical hydrodynamical model of carrier current, the equation for the self-consistent potential in the device. Current continuity is obtained as the zeroth momentum moment of the BTE, while the classical expression for carrier current represents the drift-diffusion approximation to the momentum balance equation. Momentum balance is obtained as the first momentum moment of the BTE. Poisson's equation must be solved self-consistently with the prescribed potentials applied at the boundaries and the charge density given by the other two equations.

In the high-field regime where the current response is nonlinear, the mobility and diffusion coefficient are both field dependent and must be known from laboratory measurements or from exact calculations. Recent studies have compared high-field transport behavior predicted by the semiconductor equations with more accurate solutions of the BTE (Ref. 19). These show that the conventional equations have limited utility in submicron and in high-frequency devices and are generally inaccurate in high-field transient

situations. In the classical current model, it is assumed that (1) carrier current responds instantaneously to changes in electric field, (2) the corresponding steady-state mobility and diffusion coefficient can be used at each field value, and (4) diffusion and drift do not influence each other. However, fast transient response is nonlocal in time and requires the BTE for an accurate description. The semiconductor equations are inherently unable to describe transient phenomena occurring on a time scale of picoseconds or less, as for example velocity overshoot.

A set of exact moment (or balance) equations from the BTE must be used first to obtain more accurate device equations. In one approach the electron distribution function for each energy valley is approximated by an analytic form, e.g., a Maxwellian distribution displaced in momentum space so that the average carrier momentum \bar{p}_d is along the electric field direction. The analytic form depends on a small number of time-dependent parameters (e.g., \bar{p}_d , electron temperature, and concentration) which are substituted into a like number of balance equations for the particular valley (starting with the zeroth moment equation). The resulting set of coupled equations, containing the parameters as unknowns, is used to model device behavior. Scattering integrals appearing in the balance equations may be given in approximate analytic form or evaluated numerically.

When the drifted-Maxwellian distribution is not justified, the semi-empirical transport equation method (SETEM) can be employed. In this approach one starts with the balance equations for charge, momentum and energy along with Poisson's equation. The scattering integrals in the momentum and energy balance equations are approximated with effective momentum and energy relaxation rates, respectively, which are field dependent. At each field value of interest, the relaxation rates are chosen to satisfy the steady-state form of the balance equations with exact values of steady-state drift velocity, average energy and average effective mass inserted in the equations. The exact values required are obtained from detailed numerical solutions of the steady-state BTEs, usually by Monte Carlo simulation. Thus, the SETEM attempts to describe nonstationary behavior with the steady-state parameters.

The accuracy of the more elaborate device equations just described ranges from very good to exceedingly poor, depending on the validity of the

approximations used in the particular situation treated. Surprisingly good results can be obtained, but these approaches are applicable in a limited number of cases.

The most accurate description of high-field transport behavior that is computationally tractable is the Boltzmann transport equation. Accurate numerical calculations with the BTE retain in effect the moment equations to all orders and can describe quite general temporal and spatial effects. Various numerical techniques for the solution of the BTE have been developed. Their use has been limited in the past mainly by the computational expense involved. But with the rapid development of fast large-memory computers, the cost factor is much less important now and should soon be a relatively minor consideration.

Of the various numerical approaches to the BTE, the Monte Carlo method is now by far the most popular in solid state transport analysis. It is easy to program and to include realistic band structure and scattering models. Extension to time- and space-dependent phenomena is readily implemented by an ensemble simulation. It is the only method by which fluctuation phenomena can be studied with a straightforward analysis. Being a direct simulative procedure, it is the most directly interpretable from the physical point of view. The analysis of any phenomenon on the microscopic level, i.e., in terms of band structure and scattering processes, is quite transparent. Simulation with the self-consistent field can be performed in a direct way in ensemble Monte Carlo. Inclusion of short-range carrier-carrier interactions, however, requires an elaboration of Monte Carlo that is more difficult to implement but straightforward in principle (Ref. 22). Because of its comparative advantage over other detailed numerical techniques, the application of Monte Carlo simulation to device analysis and design is increasing steadily (Ref. 17).

9.2 QUASI-CLASSICAL DESCRIPTION OF CHARGE TRANSPORT

When treating the interaction of an applied field with a material, the basic formulation of charge transport is almost always quasi-classical in nature. The mobile charge carriers in semiconductors are electrons and holes. The electron and hole systems are given a quasi-classical description in which an individual mobile carrier is assigned a Bloch energy band n and a wave-vector \bar{k} , specifying the Bloch energy state, and is simultaneously assigned

a position \bar{r} . The Bloch state has associated crystal momentum, $\bar{p} = \hbar\bar{k}$, and energy, $E_n(\bar{k})$.

The Bloch states are those of a perfect crystal lattice. As a carrier moves through the lattice, its Bloch state is randomly perturbed by crystal imperfections, namely, lattice vibrations (or phonons), impurities, structural defects, interfaces, and by other carriers. The sudden state changes are pictured as various scattering processes in which transition to another Bloch state occurs by carrier interaction with one of the perturbing sources. The scattering processes obey the laws of quantum mechanics and their cross sections are derived with the quantum theory of scattering.

In the quasi-classical description, the state of the carrier system at time t is specified by a distribution function $f_n(\bar{k}, \bar{r}, t)$ for each relevant energy band n . The number of carriers in the band at time t occupying the volume elements $d^3\bar{k}$ at \bar{k} and d^3r at r is $(2\pi)^{-3}\hat{f}_n(\bar{k}, \bar{r}, t) d^3k d^3r$ where n denotes the band (or the particular minimum of a band and possibly the spin component value as well) and \hat{f}_n is the absolute distribution function. During free flight, i.e., on a trajectory connecting two successive scattering events, the carrier motion is governed by the field acting on it and obeys the quasi-classical dynamical laws:

$$\dot{\bar{r}} = \hbar^{-1} \left(\frac{\partial E_n(\bar{k})}{\partial \bar{k}} \right) \quad (44)$$

$$\dot{\bar{p}} = \hbar \dot{\bar{k}} = \bar{F} \quad (45)$$

Here, $\dot{\bar{r}}$ is the carrier velocity in the state \bar{k} and \bar{F} is the (self-consistent) force field (apart from the periodic field of the perfect ionic lattice) in which the carrier moves between collisions.

When there is no applied field and no temperature variation, the carriers are in equilibrium with the lattice and $f_n(\bar{k}, \bar{r})$ is everywhere a Fermi-Dirac distribution with temperature equal to that of the lattice. In response to an external field the distribution changes. From the nonequilibrium distribution function at time t , all transport parameters (mean carrier energy, drift velocity, average collision rates, etc.) can be calculated at t .

The most general transport theory within the context of the quasi-classical description is essentially that embodied in the set of coupled

Boltzmann equations for the distribution functions. Of the various computational methods for analyzing charge transport in semiconductors with the full accuracy of the Boltzmann equation, Monte Carlo simulation has emerged as the most useful technique in high-field problems. Monte Carlo combines computational simplicity with the broadest applicability to complex band structures and scattering processes, and is also the most powerful method for treating problems having space dependence.

9.3 MONTE CARLO SIMULATION

In direct Monte Carlo (Ref. 21) simulation, the behavior of the physical system is simulated by computing individual particle motions. The calculated particle histories are treated as a sample set from an ensemble of histories for the particles of the physical system. The average of a particle variable over this set at a common time is an estimator for the average over the physical ensemble at that time.

For charge transport in a semiconductor, the particle (electron or hole) history (in the quasi-classical approximation) is a sequence of free flights under the influence of the electromagnetic field alternating with scatterings. Each scattering marks the termination of one free flight and the start of the next one.

Clearly a Monte Carlo computer program for charge transport calculations must contain algorithms to perform the following basic functions:

1. Describe the energy band structure, $E_n(\bar{k})$, over the full range of particle energies that are important in the problem.
2. Account for the effect of the applied field on particle motion and energy absorbed from the field.
3. Calculate the scattering function and scattering rate for each collision process as required in the simulation.
4. Statistically select, according to the scattering probability functions of the various collision processes, values of the random quantities that enter into the motion of a particle, namely, the time duration of a free flight, and the state of the particle immediately after the scattering event when the next free flight commences.

A particle simulation is started by an appropriate statistical selection of the initial position in phase space and is then allowed to proceed until the particle history is long enough (1) to include a number of scattering events that is statistically adequate for the calculation, or (2) to traverse the desired space or time interval when position or time is included in the particle variables. All the information necessary to calculate the transport quantities of interest (such as the mean particle energy or mean velocity) must be extracted and recorded from each single free flight.

In a steady-state situation with spatial uniformity, a single particle history taken over a sufficiently long time can provide the data for calculating the transport behavior. For such steady-state problems, ergodicity implies that any single long history is representative of all the particle histories in the system. Then time-averaging a variable over the particle history is equivalent to an instantaneous average of the variable over the distribution function in \bar{k} -space.

The general approach of using time averages over a single particle history is called Single-Particle Monte Carlo (SPMC). The time spent by the particle in part of \bar{k} -space is proportional to the distribution function. Setting up a mesh of cells in \bar{k} -space, a histogram may be computed which represents the time spent by the particle inside each cell of the mesh. If a mesh with sufficiently fine subdivisions and a simulation time long enough to ensure a convergent result is used, the histogram will accurately estimate the particle distribution function and can be used to calculate mean values.

Usually an average can be computed more efficiently by recording the mean value for each free flight, accumulating a sufficient number of such flights, and then averaging over all flights. This saves computer time by avoiding the histogram calculation on a mesh sufficiently fine to ensure accuracy in averaging. Other estimators for average values in steady state are given in the literature and can be more efficient than the direct cumulative average over flights (Ref. 22).

9.4 ENSEMBLE MONTE CARLO

In the case of time dependence that is neither periodic nor a simple exponential growth or decay and in most situations of spatial dependence, the simulated history of a single carrier does not adequately represent the

physical ensemble of carriers. The general approach then is to compute a large number N of particle histories, which are treated as a sample set from an ensemble of particle histories that corresponds to the actual physical system. The number N will usually be much smaller than the number of carriers in the physical system being analyzed. It need only be large enough for the system quantities of interest to be calculated accurately and without undue fluctuations as N is varied. The required value of N will depend on the particular problem.

To allow for interaction between particles (see *Collective Effects*, Section 9.10), the particle histories are computed in parallel. For each particle, the initial Bloch state (and position also when there is spatial nonuniformity initially) is selected by sampling the initial distribution of the physical system. For each particle, the values of the set of recorded particle variables at a designated observation time are used to estimate the desired transport quantities from appropriate averages over the N particles. This gives estimates of these transport parameters (with possible spatial variation) at the average time associated with a set of observation times. In the next cycle of the computation, an increment of each particle history is generated corresponding to a time step.

The evolution of this simulation at successive time steps represents the actual time dependence. This is referred to as the Many-Particle Ensemble Monte Carlo (MPEMC) scheme. For combined time and space dependence, i.e., transient dynamic response that is dissimilar at different space points, MPEMC offers the only tractable approach to the Boltzmann equation.

The true time scheme has been adopted as the procedure for implementing the program cycles that generate the time steps. In this procedure, the particle histories are computed between successive observation times, $t^{(1)}$, $t^{(2)}$, ... that are predetermined and are the same for each particle. The time steps $\Delta t = t^{(p+1)} - t^{(p)}$ can all be equal, or can be spaced more closely for one part of the time range than another as deemed advisable. With all N particle states known at time $t^{(p)}$, for each particle in turn a Monte Carlo procedure is used to compute the further history up to time $t^{(p+1)}$. First, a free-flight time t is chosen for the particle and $(t^{(p+1)} + t)$ is compared with $t^{(p+1)}$. The particle trajectory is then computed up to the lesser of these two times. If a scattering occurs within the time interval Δt , the

result of the collision and the new flight time following the collision are obtained by statistical selection procedures in the program. The process is repeated until $t^{(p+1)}$ is reached. It is unnecessary to continue the same free flight from before an observation time to after. The particle must have the same wave vector \bar{k} and position \bar{r} just after the observation time $t^{(p)}$ as just before, but it can be assigned a new flight time commencing at $t^{(p)}$. Thus, the remainder of the flight duration at the observation time $t^{(p)}$ (on the flight which the particle was following when it reached $t^{(p)}$) need not be stored for each particle. The values of the particle variables at time $t^{(p)}$ are stored for all N particles, and transport quantities or interparticle effects are calculated for this time. Thus, the scatterings and flights are computed in essentially the same way as in SPMC, except that the basic segment of a particle's history is the interval Δt between observation times rather than the (variable) interval between scatterings. Each segment concludes at an observation time, and the next one begins at this time. The computer time required will depend mainly on the number of scatterings rather than the number of observation times.

9.5 ENERGY BAND STRUCTURE

For a cubic type semiconductor, the momentum vectors at the energy minima of a conduction band are located at the center Γ ($\bar{p} = 0$) and on the symmetry axes (Δ along the $[1, 0, 0]$ directions and Λ along the $[1, 1, 1]$ directions) of the first Brillouin zone. Near a minimum point \bar{p}_0 , the $E(\bar{p})$ energy function can be approximated by terms to second order of a Taylor expansion about \bar{p}_0 , i.e., by a quadratic function of $(\bar{p} - \bar{p}_0)$. The quadratic form is called the parabolic approximation to $E(\bar{p})$ or the effective mass approximation. The corresponding surfaces of constant energy centered at Γ are spheres while those centered at a minimum on a Δ or Λ axis are generally ellipsoids of revolution having a common symmetry axis along the particular Δ or Λ axis. The two upper valence bands have degenerate maxima at Γ . The equienergetic surfaces about Γ are to second order in the components of \bar{p} , more complicated warped surfaces.

Further up the energy valley centered at the minimum point \bar{p}_0 of a conduction band, the energy function deviates from a simple quadratic expression. An energy-momentum relation accurate to larger values of $(\bar{p} - \bar{p}_0)$, into the region of nonparabolicity, is obtained through the relationship

$E(\bar{p}) = E(1 + \alpha E)$, where $E(\bar{p})$ on the left denotes the quadratic function of momentum characterizing the parabolic approximation and α is the nonparabolicity parameter. This device accounts partly for the nonparabolicity of the band structure at energies further up the valley.

These relatively simple approximations of band structure are adequate for electron energies up to about 0.5 eV above a valley minimum. They have been widely used in transport calculations. In Monte Carlo simulation they give agreement with experiments for electric fields up to approximately 10 kV/cm. The values of the parameters entering into the expressions (effective masses, energy values at extrema, location of energy minima on Δ axes, nonparabolicity parameters, valence-band warped surface parameters) are well established for all the important cubic semiconductors of Group IV elemental type and III-V compound type.

The present form of the ensemble Monte Carlo program allows any analytic approximation for the energy band function to be used. This has been accomplished with relatively simple programming compared to the method used heretofore for ellipsoidal energy surfaces (Ref. 23). The algorithm used exploits the high symmetry of the first Brillouin zone in cubic crystals.

The set of momentum vectors specifying the Bloch states of an energy band can be chosen to lie in the volume of momentum space called the first Brillouin zone. The zone is centered at the origin and has symmetry properties reflecting the spatial symmetry of the crystal lattice. For a cubic crystal, it has the symmetry of a cube. To any momentum vector \bar{p} there correspond 47 other momentum vectors in the Brillouin zone having exactly the same energy value $E(\bar{p})$. The 48 vectors are related by the 48 symmetry operations of the cube.

This symmetry of the band structure can greatly facilitate the use of analytic expressions corresponding to extremum points in a relatively small part of the Brillouin zone, namely, in an irreducible wedge comprising (1/48) of the total volume. To determine the energy value for an arbitrary momentum vector of the Brillouin zone, it is transformed by the appropriate symmetry operation into the corresponding vector of the irreducible wedge. The analytic approximation for the energy about the nearest extremum point in the wedge is then used to calculate the energy.

9.6 REALISTIC BAND STRUCTURE

At electron energies of 1 eV or more above the minimum point of an energy valley in the conduction band, the approximate analytic expression for the energy function is very inaccurate. Hence, for electric fields at which average electron energies exceed 0.5 eV, more accurate band structure becomes necessary. Furthermore, at even lower electron energies, interband transitions to the second conduction band begin to have an effect. Then the Monte Carlo simulation must include interband as well as intraband scattering involving the first two or more conduction bands.

For electric fields above 100 kV/cm, the number of carriers whose energy exceeds the valence-conduction bandgap starts to be significant. Another carrier collision process, impact ionization, then becomes important. Impact ionization involves relatively few carriers in the distribution, those occupying the comparatively small high-energy tail. Calculation of ionization rates, however, requires a fairly precise determination of their energy distribution. Hence, realistic band structure is a necessity.

Energy bands can be calculated precisely by various advanced methods. Of these, the empirical pseudopotential method has been found to be the most useful for transport problems. Shichijo and Hess (Ref. 23) were the first to employ realistic band structure in Monte Carlo simulation. Band structure symmetry also facilitates the use of computed energy values, since the energy and momentum gradient of energy need be tabulated only at a mesh of points in an irreducible wedge. Again, an arbitrary momentum vector in the Brillouin zone is transformed into the corresponding vector in the wedge. The desired energy value is obtained from a weighted average of the energies at the mesh points surrounding the transformed momentum vector.

9.7 SCATTERING RATES

In addition to the energy-band structure, Monte Carlo simulation of charge transport in a semiconductor crystal requires the scattering rates of the various carrier interaction processes. Both properties of the material must be known fairly precisely at all carrier energies of importance in the distribution function for the field strength considered. In general, this becomes more difficult as field strength increases and produces higher carrier energies.

Many high field effects occur at electric fields $F < 50$ kV/cm. Within this range it is usually adequate to treat electron transport with only the first conduction band and approximate analytic energy functions. Scattering rates are calculated using ordinary perturbation theory with the energy density of states given by the approximate band structure. The resulting angular dependence and total scattering rates of the various scattering mechanisms have been extensively applied in Monte Carlo calculations.

They give good agreement with measured high-field transport behavior at electric fields below 50 kV/cm, where the range of significant electron energies lies below 1 eV. Thus, the low energy scattering rates, valid for electron energies below 1 eV, are now well established for the important semiconductor materials.

Analytical expressions giving the scattering rates in the low energy approximation are available in the literature for all the important scattering mechanisms. These include intravalley scattering by acoustic phonons and by polar and nonpolar optical phonons. In intervalley scattering, the electron is scattered from one valley to another in the same band, either an equivalent valley or an inequivalent one (the latter has a minimum energy different from that of the initial valley). Intervalley phonon scattering is induced by acoustic or nonpolar-optical phonons of rather large energy. It becomes important at electron energies high enough for emission of these phonons to be energetically possible. In piezoelectric crystals, intravalley scattering by acoustic piezoelectric phonons can be appreciable.

Nonphonon scattering mechanisms often important are ionized impurity and neutral impurity scattering. The latter can also cause intervalley scattering. In ternary alloys, A,B,C intravalley alloy scattering must be considered when the mole fraction x of the binary AC is not close to the value zero or one. Alloy scattering can be viewed as arising from randomly distributed potential wells against a uniform periodic background. These wells occur at the lattice sites associated with one of the alloying constituents, say B, and represent the difference in ionic potentials at sites occupied by ion cores of A and B.

In impact ionization the interaction of a mobile carrier with a valence electron causes a transition of the latter to the conduction band, so the

final state has an electron-hole pair in addition to the primary carrier. The process has an energy threshold that is not less than the bandgap energy. It is important for fields exceeding 100 kV/cm, where the number of electrons with energy above threshold becomes significant.

A scattering function calculated by perturbation theory is proportional to the energy density of final states. The density of states obtained from the effective mass approximation is customarily inserted into the calculation. However, this approximate density continually increases with energy, whereas the true density of states peaks at some energy E_c and thereafter falls off. The true density can be taken as that given by the realistic band structure calculation. For electron energies below E_c , the true and approximate densities increase with energy and agree over much of the interval. The perturbation-theoretic scattering rates of nonpolar phonon processes as well as the total scattering rate increase with energy below E_c in agreement with established values for the rates. However, these rates continue to increase indefinitely with energy, contrary to more accurate calculations which show a fall off in the vicinity of E_c . In practice the scattering rates from perturbation theory, with coupling parameters adjusted to give agreement with observed transport behavior up to the lower range of high fields, can be used for electron energies below E_c . At higher energies the scattering rates are modified in accordance with calculated rates that are based on non-perturbative field-theoretic methods and use the true density of states (Ref. 23 and 24).

9.8 QUANTUM EFFECTS

At electron energies about 1.5 eV above the conduction band edge, quantum-mechanical effects become important in semiconductor transport. At these energies, the number of electron states per unit energy range is high and the scattering rates of many phonon collision processes are large. As dictated by the energy-time uncertainty effect, scattering introduces uncertainty into the electron energy. At the highest scattering rates the energy uncertainty is not necessarily small compared to the energy itself.

In the quasi-classical Boltzmann equation description, the energy eigenstates of the unperturbed electron are used in defining the distribution function. But when the electron interacts strongly with lattice phonons, it is more accurately described as propagating in a perturbed state. In a

perturbed state the electron continually emits phonons and reabsorbs them by virtual collision processes. As a result of the interactions, the state has a range, ΔE , of energy values and an energy center displaced from the sharp energy value of the corresponding Bloch state.

Much of the incorrect nature of the quasi-classical Boltzmann equation can be removed by introducing the concepts of a quasi-particle and its self-energy. The quasi-particle is the Bloch electron with its accompanying cloud of virtual phonons. The self-energy corresponds to a mass renormalization and can be calculated by field-theoretic operator techniques. The real part of the self-energy is equal to the level shift and the imaginary part is equal to the collision-broadened width, ΔE , of the level. Also, the total scattering rate (in real collisions) of the quasi-particle is directly proportional to its level width, ΔE , from collision broadening, in accordance with the uncertainty effect.

Recently it has been shown by H. Shichijo and K. Hess (Ref. 23) and by J.Y. Tang and K. Hess (Ref. 24) for gallium arsenide and silicon, respectively, that the accuracy of impact ionization rates calculated by the Monte Carlo method is significantly improved by introducing the quantum effects described above. In the simulation, the particle is scattered into a range of final energies corresponding to the widths of the initial and final quasiparticle states. Moreover, the total scattering rate at energies above E_c is chosen in accordance with the energy dependence of the rate given by the self-energy calculation. For carrier energies below E_c the perturbation-theoretic scattering rates are used, and the high energy rates are joined continuously onto these.

9.9 TIME-OF-FLIGHT ALGORITHMS

A free-flight time is the interval between successive collisions, during which the electron drifts under the influence of the field. The algorithm that selects the flight times is one of the most important features of a Monte Carlo computer program. A better method improves the speed of the program and the accuracy of the simulation. For our purposes, the procedure must be relatively easy to implement even with a complicated energy-band structure, such as that seen by the higher energy electrons of the distribution.

Another consideration is compatibility with spatial dependence. In the operation of many devices, carrier transport varies with position in space. This arises from material nonuniformity and interfaces or from prescribed boundary conditions, such as carrier injection at a junction or a heterojunction barrier. Often a nonuniform field occurs. Hence, it is desirable that the algorithm be adaptable to the case of a rapidly varying field.

Let $\nu(t)$ be the total collision rate of an electron at time t along the path of a free flight. The probability of the electron being scattered in the time interval $(t, t + \Delta t)$ can be taken as

$$P_{sc}(t, \Delta t) = \nu(t) \Delta t \quad (46)$$

provided Δt is short enough for $\nu(t)$ to be essentially constant over the interval. It follows directly that the probability of the electron drifting without collision from $t = 0$ to $t = T$ is

$$P(T) = \exp - \int_0^T (\nu \bar{p}(t)) dt \quad (47)$$

The cumulative probability that the free-flight time lies somewhere in the time interval $(0, T)$ is $1 - P(T)$, which has the value 0 at $T = 0$ and approaches the value 1 for large T . Free-flight times having the required probability distribution can be selected as follows: Generate a random number r , uniformly distributed between 0 and 1 and solve

$$r = 1 - P(T) \quad (48)$$

for t , which is taken to be the free-flight time. However, the collision rate is a complicated function of the time along the electron's free trajectory, and there is no direct way of inverting Equation 48 to obtain T . Each selection of a flight time involves a numerical integration, as shown in Equation 47.

Two alternative methods are available. The most commonly used device is to introduce self-scattering, a fictitious process which leaves the electron state unchanged but serves to make the total scattering rate (including self-scattering) a constant for all electron states, $\bar{\nu}$. Then, the right-hand side of Equation 47 becomes a simple exponential function of T and Equation 48, and is easily inverted to express T as a logarithmic function of r . The drawback to the self-scattering scheme is evident at energies where the total

of the real processes is relatively small and the self-scattering rate is then necessarily large. As a result, an inordinate amount of computer time is spent on self-scattering events which have no physical significance. To improve the efficiency of the simulation, one can divide momentum space into energy regions and assign optimum values to the total scattering rate in each region. The method works well if simple analytical expressions for the energy surfaces can be used, as is the case at field strengths where the electrons are concentrated mainly in the lower regions of the energy valleys. But when realistic band structure is required, as at high electron energies, the subdivision into energy regions becomes intractable.

The most utilitarian device dispenses with the integral form of Equation 48 and utilizes the differential form of Equation 46. The procedure is the following. Consider an electron in free flight at time t . First calculate the total scattering rate $\nu(t)$ for the state of the electron at this time. The random number r , uniformly distributed between 0 and 1, is generated to decide whether the electron is scattered in the next time increment Δt . If r satisfies $r \leq \nu(t)\Delta t$, proceed to scatter the electron at $t + [r/\nu(t)]$. Otherwise, continue its free flight to time $t + \Delta t$, at which time the entire process is repeated. Experience reported with this method (Ref. 24) indicates that as long as Δt is chosen to be about one tenth the mean scattering time in the current region of momentum space, both the speed and the accuracy of the computation are satisfactory. The differential scheme has the following advantages: (1) no complications arise from the complexity of the energy surfaces, and (2) a simple generalization makes it applicable to spatially varying fields (where the integral method is unsuitable).

9.10 COLLECTIVE EFFECTS

When carrier concentrations are high, charge transport can be strongly influenced by collective effects. These arise from interaction among the particles and the resulting many-particle correlations. It is convenient to resolve the interaction between carriers into two parts. One part, described as carrier-carrier scattering, accounts for the strong short-range coulomb interaction between an individual pair of particles in the immediate vicinity of one another. Each carrier-carrier collision conserves the total energy of the pair but exchanges energy between them. The collisions are effective in

equilibrating the carrier energy distribution. This type of scattering must be included in the Monte Carlo simulation at large carrier densities to describe the strong tendency toward thermalization of the carrier distribution under these conditions. Clearly a many-particle ensemble Monte Carlo scheme is required.

The other part of the carrier-carrier interaction is included in the space-charge effect and describes the average continuous influence on any single carrier of all the others. This accounts for the long-range part of the coulomb interaction and contributes to the total field acting on a carrier. The field in the material is the result of both the external applied potentials and the spatial distribution of charge from both the carriers and the background of ionized impurities. The resulting self-consistent electric field can be calculated by Poisson's equation when the charge distribution is known.

The MPEMC scheme is well suited to the analysis of collective effects. As an example, consider carrier-carrier collision (Ref. 22). Two carriers enter a mutual scattering in the initial states (\bar{p}_1, \bar{p}_2) and emerge in the final states (p_1', p_2') with probability equal to $S_2(\bar{p}_1, \bar{p}_2; \bar{p}_1', \bar{p}_2')$, where S_2 is the pair scattering function. The final states (\bar{p}_1', \bar{p}_2') are those allowed by energy and crystal-momentum conservation. Integrating S_2 over the entire \bar{p} -space of the variables \bar{p}_1', \bar{p}_2' gives $\tau_2(\bar{p}_1, \bar{p}_2)$, the total mutual scattering rate for the initial pair (\bar{p}_1, \bar{p}_2) . For carrier 1, the scattering probability per unit time for this process at time t is proportional to $\tau_2(\bar{p}_1, \bar{p}_2) f(\bar{p}_2, \bar{r}, t)$. Each carrier (and each impurity ion) has its coulomb field screened by local adjustment of the mobile charges in its vicinity. Hence, S_2 describes scattering by a screened coulomb potential (i.e., similar to charged impurity scattering). The microscopic details of the screening depend on the carrier distribution function in the neighborhood of the charge and an exact treatment is complicated in nonequilibrium situations.

The carrier-carrier scatterings are calculated using the distribution function obtained at the preceding observation time. In a situation of spatial uniformity, the momentum distribution of neighboring carriers can be estimated by sampling from the states of all the other carriers in the ensemble at the observation time. The observation times may be made as frequent as necessary

for this purpose with an addition to computer time that does not include additional single-particle scattering computations. The screening is treated approximately by Debye theory, which is valid in equilibrium. Simulation of carrier-carrier scatterings over the segment of each particle history that occurs in the time interval between $t^{(m)}$ and $t^{(m+1)}$ can be done with the following successive steps:

1. Consider particle 1 in free flight in this interval. Choose a companion state \bar{p}_j randomly from the other $N-1$ particle states in memory storage at the observation time $t^{(m)}$.

2. Consider any statistical selection involved in choosing the duration or the type of terminating collision for this flight. Use the pair (\bar{p}_1, \bar{p}_j) as the initial states and $\tau_2(\bar{p}_1, \bar{p}_j)$ as the scattering probability of a mutual scattering by particle 1, where \bar{p}_1 is the momentum of particle 1 at the time in the free flight at which the statistical selection is being made. (See Section 9.9.) Of course, the competing single-particle scattering probabilities used at this time are those evaluated at \bar{p}_1 .

3. If Step (2) results in a mutual scattering, then select values of (\bar{p}_1', \bar{p}_j') in accordance with the distribution given by $S_2(\bar{p}_1, \bar{p}_j; \bar{p}_1', \bar{p}_j')$.

4. Repeat Steps (1) to (3) for all the flight/scattering cycles required for particle 1 to reach the observation time $t^{(m+1)}$. If the probability of a mutual scattering is relatively small compared to the other processes, Steps (1) to (3) may be executed in only a fraction of the flight/scattering cycles while replacing τ_2 in Step (2) by τ_2/a .

5. Repeat Steps (1) to (4) for particles 2, 3, ..., N .

Due to the long range of the coulomb force, each charge carrier feels, to some extent, the presence of all other carriers and all impurity ions in the device. These other charges contribute to the total field (beyond that of the perfect ionic lattice) acting on the carrier in free flight. Because of the large number involved, their net contribution to the field acts in a continuous manner and is determined by the macroscopic spatial distribution of charge, the sum of the charge distributions given by the carrier density function and the density distribution of impurity ions.

The space charge effect can be included in the computation when particle positions are recorded. The carrier density function at a particular time is estimated from the location of particles in the carrier ensemble at that time. The total self-consistent potential at $t^{(m)}$ is calculated by solving Poisson's equation with the space charge distribution at $t^{(m)}$ and the prescribed potentials applied at the spatial boundaries. In the time step to the next observation time $t^{(m+1)}$, all free flights are presumed to be governed by this potential. At the next observation time, the self-consistent field is recalculated.

9.11 NEGATIVE DIFFERENTIAL CONDUCTIVITY

Differential conductivity is the rate of change of current density, J , with electric field, F . Negative differential conductivity (NDC) can arise from various mechanisms in the bulk or in connection with junction phenomena. It shows two distinct forms of behavior.

In voltage-controlled manifestations of NDC, the curve of J versus F has a shape resembling an N. Beyond the threshold value of F , the curve has a negative slope and NDC continues to some larger value of F beyond which the slope turns positive again. Bulk NDC of this type occurs at high fields in GaAs and other polar semiconductors as a transferred-electron effect. With a short length of material in the appropriate external circuit, a transient instability occurs in which a region of high field and charge accumulation forms. The region has the structure of a layer transverse to the electric field and propagates at the speed of the applicable drift velocity. As soon as the layer disappears at the anode side, a new layer forms at the cathode side. The domain propagation is utilized in the Gunn oscillator.

In current-controlled NDC, the curve of J versus F has the approximate shape of an S and J is a multivalued function of F . The differential conductivity at some point starts to rise with increasing field. At some break-over value of F , an instability in J develops and a small further increase in J is accompanied by a switch from a high- to a low-field region. This form of NDC leads to the formation of a high-current filament running along the field direction. The constriction of the current results in local heating of the material and further increase in current. If the current is allowed to increase in this breakdown regime, melting in the filament region will damage

the device. Analysis has begun using Monte Carlo simulation to determine if current-controlled NDC can occur in the bulk from a transferred electron effect. This could provide basic understanding of second breakdown (Refs. 1, 25 and 26), the damage mechanism commonly observed at very high fields.

10.0 MONTE CARLO ANALYSES AT VERY HIGH FIELDS

Monte Carlo simulation of nonlinear transport at fields in the range from 100 to 1000 kV/cm have been performed in collaboration with Professor K. Hess and T. Wang at the University of Illinois-Urbana, Illinois, under subcontract to Rocketdyne*. The analysis addresses some basic questions concerning the physics of second breakdown in bulk semiconductors and is the first accurate modeling of its transport behavior. Professor Hess has pioneered in the extension of Monte Carlo calculations to high fields. His group has developed and applied computer programs containing many of the refinements required, particularly realistic band structure and accurate scattering rates at high energies. Hence, his interest and involvement in the study has enabled us to carry out reliable calculations within the time limits set.

The numerical simulations were performed for electron transport in GaAs, Si and InP and used the most complete Monte Carlo program presently in existence. The calculations simulate electron motion and multiplication (impact ionization), the empirical pseudopotential method. All scattering mechanisms relevant at high energies are included in the simulation. Band-structure changes with temperature are also taken into account. The basic questions, raised by M.E. Snyder, are the following:

1. Can electrons escape to higher conduction bands exhibiting higher mobility? In other words, is it possible that at very high electric fields and/or during short times the current does not saturate or decrease but increases with electric field even if the carrier concentration were to remain constant?
2. Is it possible for high level current injection to be augmented by ballistic transport during short times?
3. Does avalanche breakdown, as often conjectured previously, generally die out as the temperature increases?
4. Is the temperature dependence of negative differential conductivity (NDC) adequate enough to support microplasma formation and growth alone?

* Rockwell International Corporation

10.1 RESULTS FOR ITEM 1

The answer is yes. A clear increase in drift velocity can be seen for GaAs (Figs. A4, A7) and for InP (Figs. A13, A16) at higher temperatures. But no increase is computed for Silicon (Fig. A1) up to 10,000 kV/cm. Thus, the process appears to be very complicated and highly dependent on the material, i.e., on specific band structure and scattering-rate details.

10.2 RESULTS FOR ITEM 2

Typical scattering rates at high energies as given by the numerical simulations were investigated. The results show that a possibility exists for ballistic motion after the electrons have attained sufficient energy to overcome the maximum in the density of states (DOS), (Fig. A2). At these high energies ballistic motion may persist for picoseconds, while at the energy of highest density of states the ballistic transport is limited to less than 0.01 ps.

10.3 RESULTS FOR ITEM 3

Surprisingly, the result is no. Avalanche breakdown does not die out as the temperature increases. It only becomes weaker in a small temperature range up to about 400 K or 500 K in the case of GaAs (Fig. A3). At higher temperatures the rate becomes stronger (Figs. A5, A12, A15). The reason seems to be a quantum mechanical renormalization which does not let the scattering rates grow with temperature much above their peak value at the point of the highest DOS. It is the almost constant peak value which is responsible for the ionization rate. This result, however, is preliminary and needs to be carefully checked.

10.4 RESULTS FOR ITEM 4

The answer is no, as can be seen from the magnitude of the temperature variations in Sections 10.1 and 10.3.

REFERENCES

1. Snyder, M.E., The Physics of Second Breakdown, AFWL-TR-83-22, Air Force Weapons Laboratory, Kirtland Air Force Base, New Mexico, pp. 7-8, Nov 1983.
2. Bower, R., and Steele, M.C., "Plasma Effects in Solids," Proc. of the IEEE, Vol. 52, p. 1105, Oct 1964.
3. Platzman, P.M., and Wolff, P.A., "Waves and Interactions in Solid State Plasmas," Solid State Physics, Supp. 13, Academic Press, New York, New York, 1973.
4. Bloembergen, N., et al, "Laser-Induced Electric Breakdown in Solids," IEEE Joul. of Quant. Elec., Vol QE-10, No. 3, p. 375, Mar 1974.
5. Chen, F.F., Introduction to Plasma Physics, Plenum Press, New York, New York, pp. 1-4, 1974.
6. Bube, R.H., Electronic Properties of Crystalline Solids, Academic Press, New York, New York, pp. 121-160, 1974.
7. Kittel, C., Introduction to Solid State Physics, Fifth Edition, John Wiley and Sons, New York, New York, Table 2, p. 223, 1976.
8. Bube, R.H., IBID, pp. 468-469.
9. Bennett, W.H., "Magnetically Self-Focusing Streams," Phys. Rev., Vol. 45, p. 890, Jun 1934.
10. Willardson, R.K., et al, "Plasmas in Semiconductors and Semimetals," Semiconductors and Semimetals, Vol. 1, Academic Press, New York, New York, pp. 444-447, 1966.
11. Seshadri, S.R., Fundamentals of Plasma Physics, American Elsevier Publishing Company, pp. 125-127, 1973.
12. Boyd, G.D., et al, "Excitation of Plasma Oscillations and Growing Plasma Waves," Phys. Rev., Vol. 109, p. 1398, 1958.
13. Pines, D., and Schrieffer, J.R., "Collective Behavior in Solid State Plasmas," Phys. Rev., Vol. 124, No. 1, p. 1387, Dec 1961.
14. Willardson, R.K., et al, IBID, p. 478.
15. Ancker-Johnson, B., and Drummond, J.E., "Thermal Pinching in Electron-Hole Plasma," Phys. Rev., Vol. 131, No. 5, p. 1961, Sep 1963.
16. Chen, W.S., and Ancker-Johnson, B., "Pinch Oscillations in Electron-Hole Plasmas, I. Theory and II. Experiment," Phys. Rev. B., Vol. 2, No. 11, pp. 4468 and 4477, Dec 1970.

REFERENCES (Concluded)

17. A general survey of recent developments is given in "The Physics of Submicron Structures," edited by Grubin, H.L., Hess, K., Iafrate, G.J. and Ferry, D.K., Plenum Press, New York, New York, 1984.
18. Hess, K., Advances in Electronics and Electron Physics, Vol. 59, pp. 239-291, 1982.
19. Sze, S.E., "Physics of Semi-conductor Devices," Second Edition, Wiley-Interscience, New York, New York, p. 298, 1981.
20. Grubin, H.L., Ferry, D.K., Iafrate, G.J. and Barker, J.R., VLSI Electronics: Microstructure Science, Vol. 3, Academic Press, New York, New York, 1982.
21. Jacoboni, C. and Reggiani, L., Rev. Mod. Phys., Vol. 55, pp. 643-705, Jul 1983.
22. Price, P.J., Semiconductors and Semimetals, Vol. 14, Academic Press, New York, pp. 249-308, 1979.
23. Shichijo, H. and Hess, K., Phys. Rev. B, Vol. 23, pp. 4197-4207, Apr 1981.
24. Tang, J.Y. and Hess, K.J., Appl. Phys., Vol. 54, pp. 5139-5144, Sep 1983.
25. Portnoy, W.M., "Reverse Bias Second Breakdown in Power Switching Transistors," AFWL-TR-82-139, Air Force Weapons Laboratory, Kirtland Air Force Base, New Mexico, May 1983.
26. McMullen, S.A. and Portnoy, W.M., "Energy Considerations in Second Breakdown," AFWL-TR-84-111, Air Force Weapons Laboratory, Kirtland Air Force Base, New Mexico, Feb 1985.

APPENDIX

GRAPHS AT UNIVERSITY OF ILLINOIS-URBANA MONTE CARLO RUNS

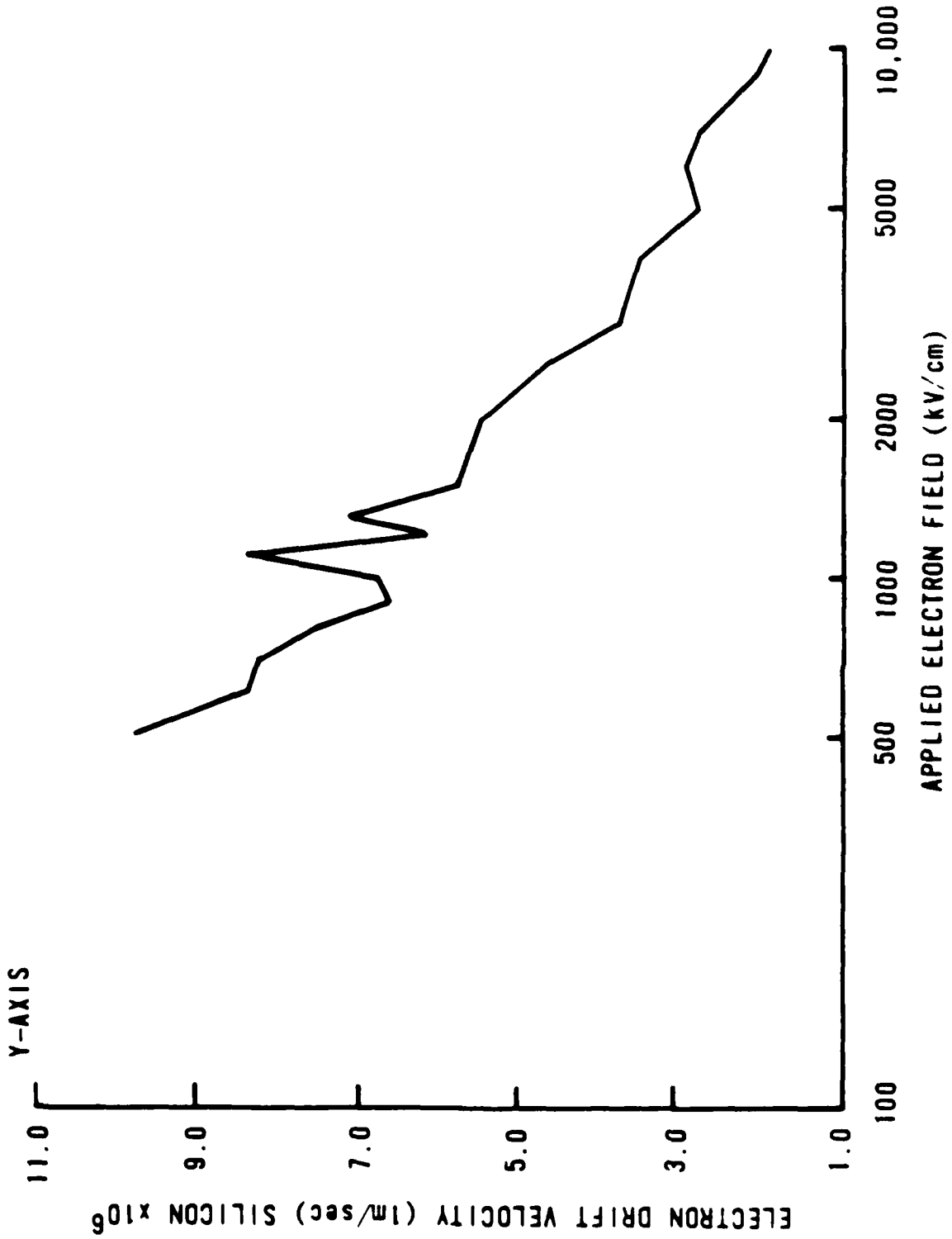


Figure A1. Electron drift velocity versus applied electric field in silicon.

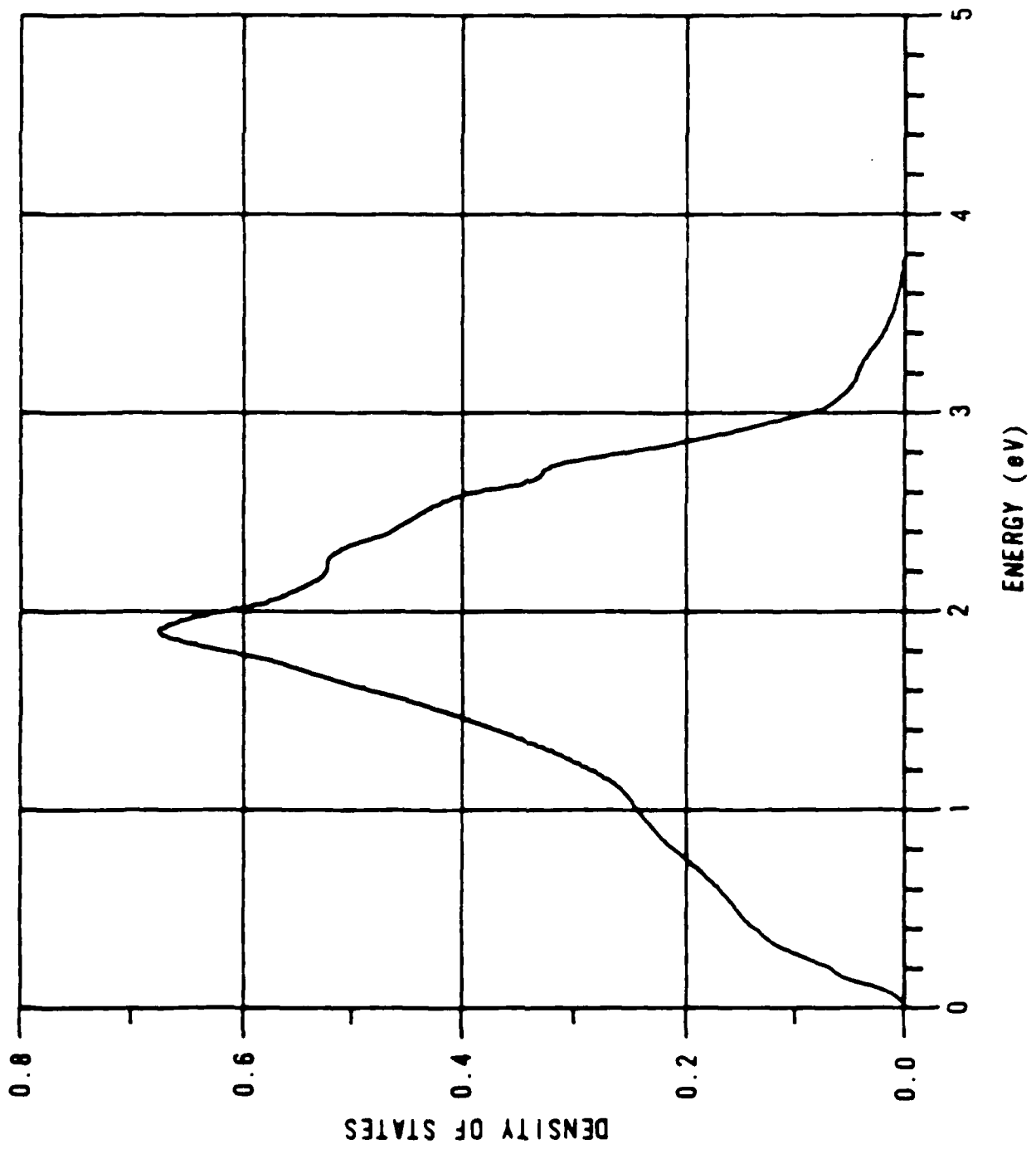


Figure A2. Density of states versus energy in silicon's conduction band.

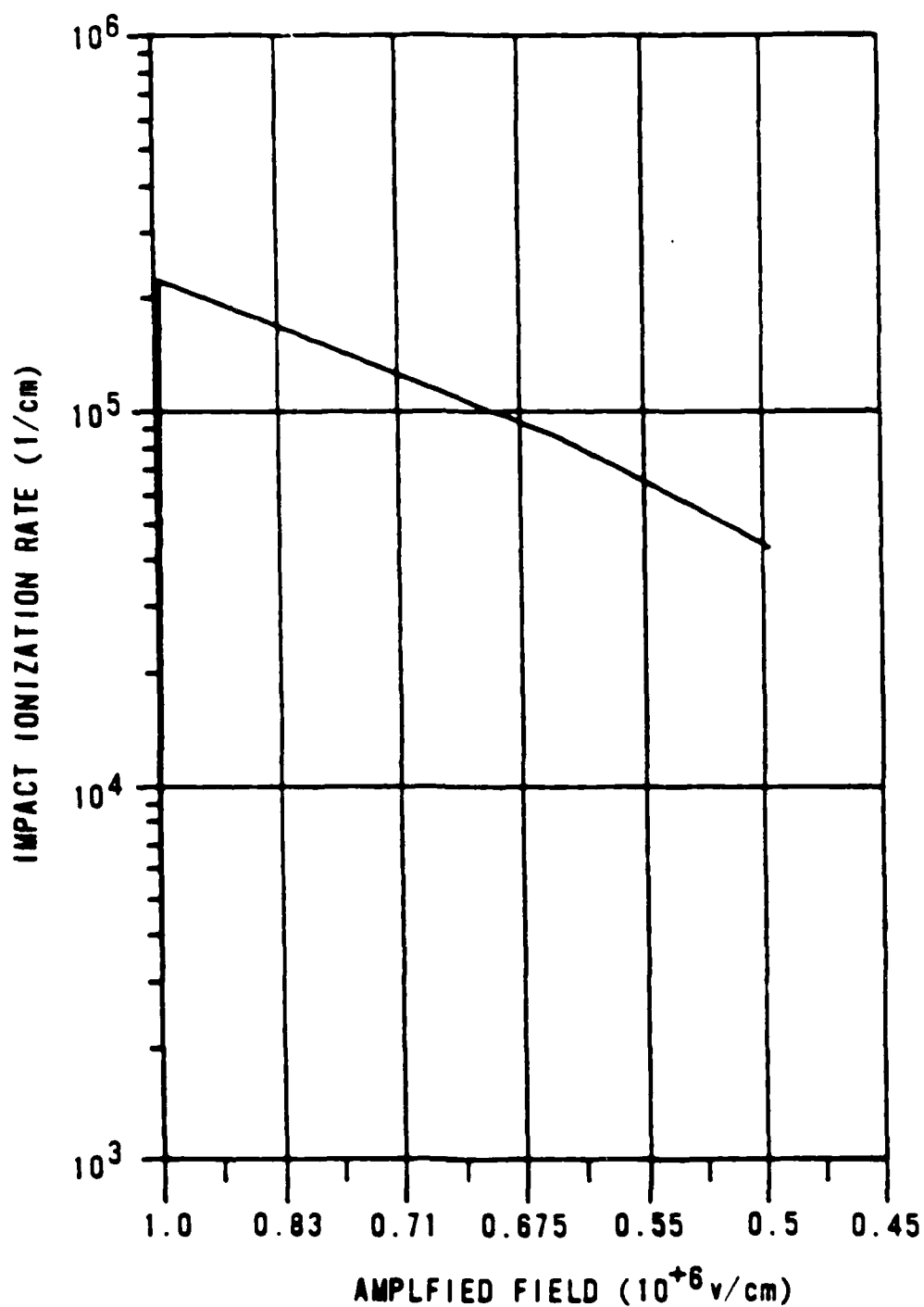


Figure A3. Impact ionization rate versus applied field in GaAs at $T = 500$ K. Coupling constant is 0.024.

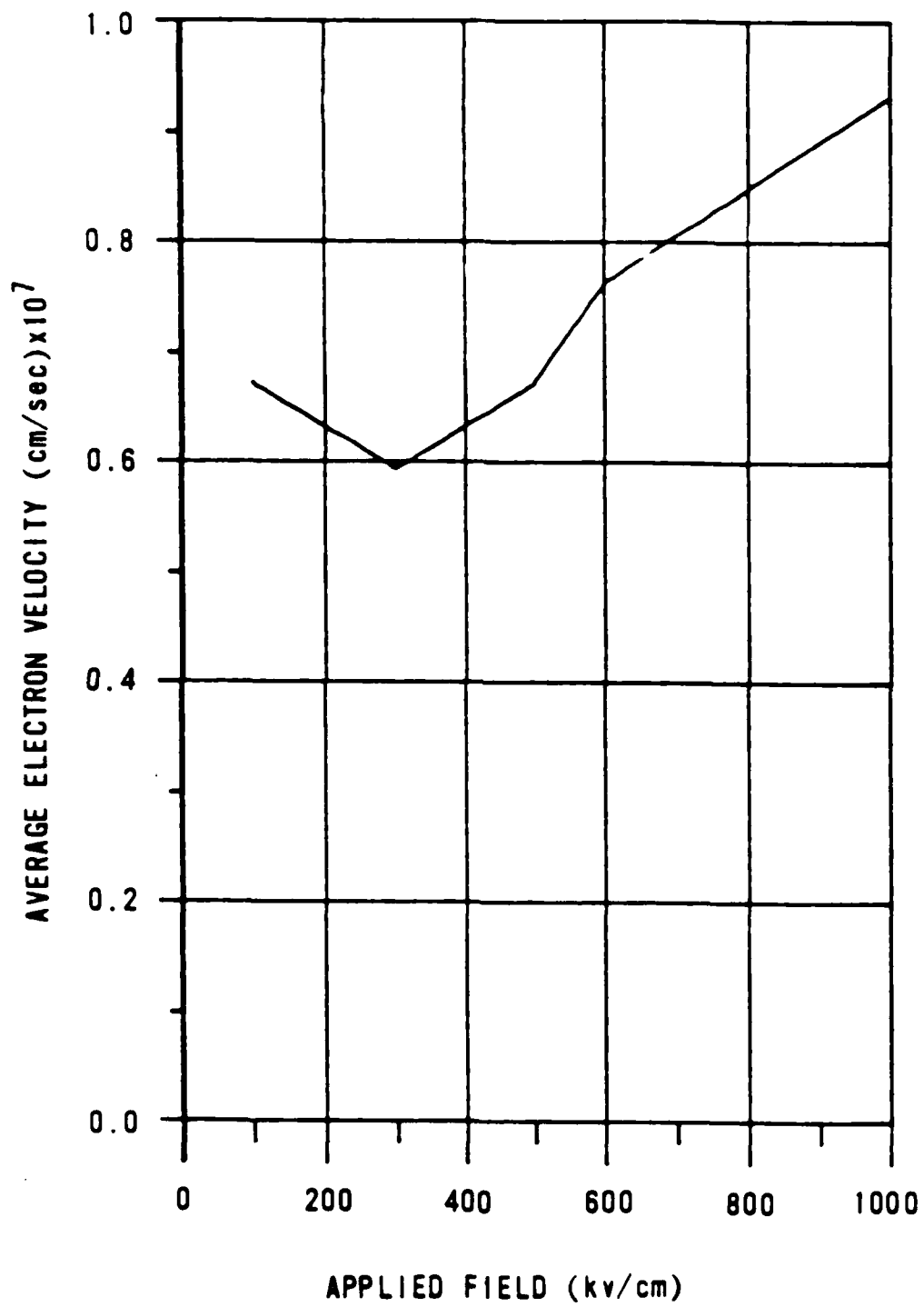


Figure A4. Average electron velocity versus applied field in GaAs at T = 500 K.

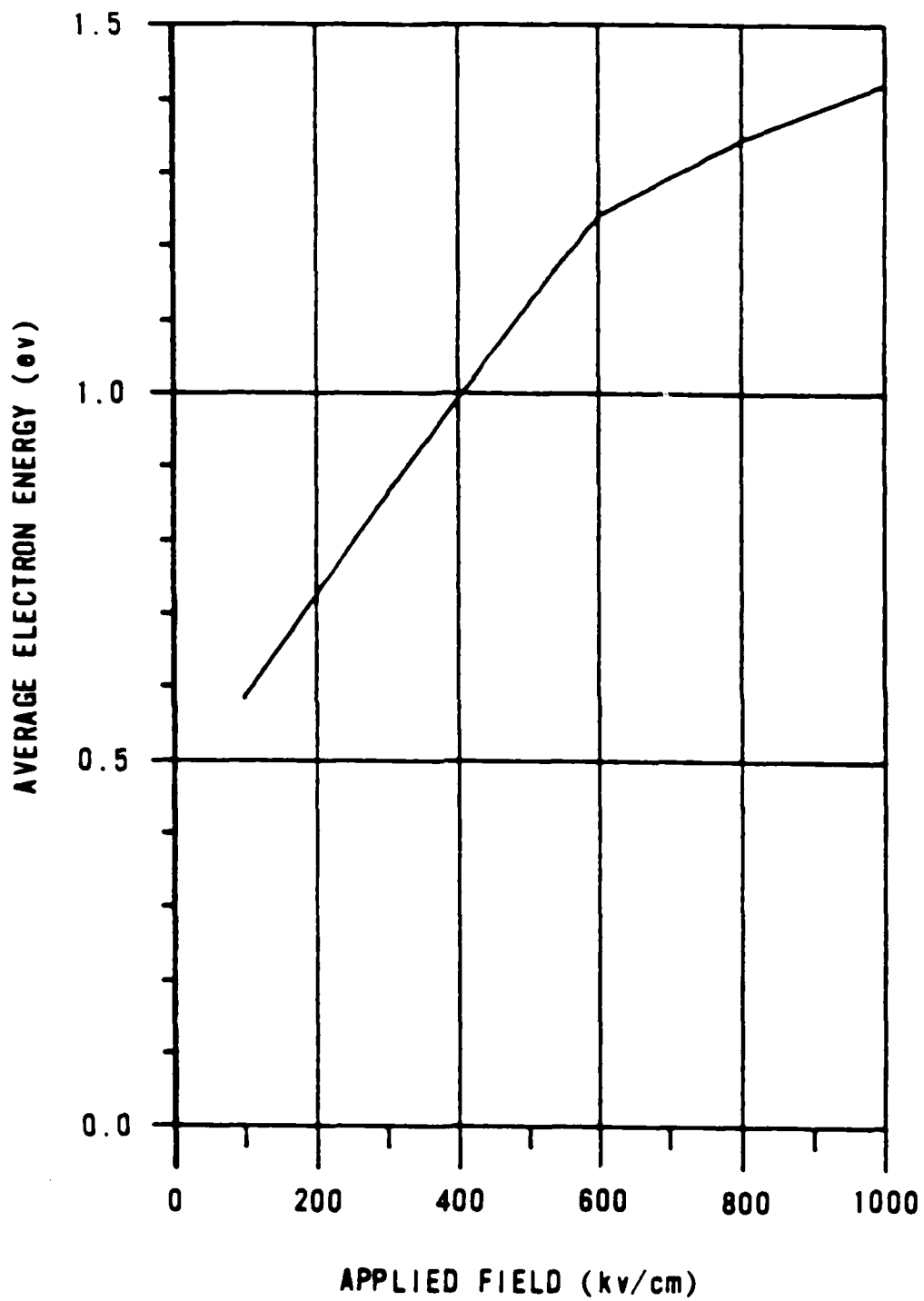


Figure A5. Average electron energy versus applied field in FaAs at T = 500 K.

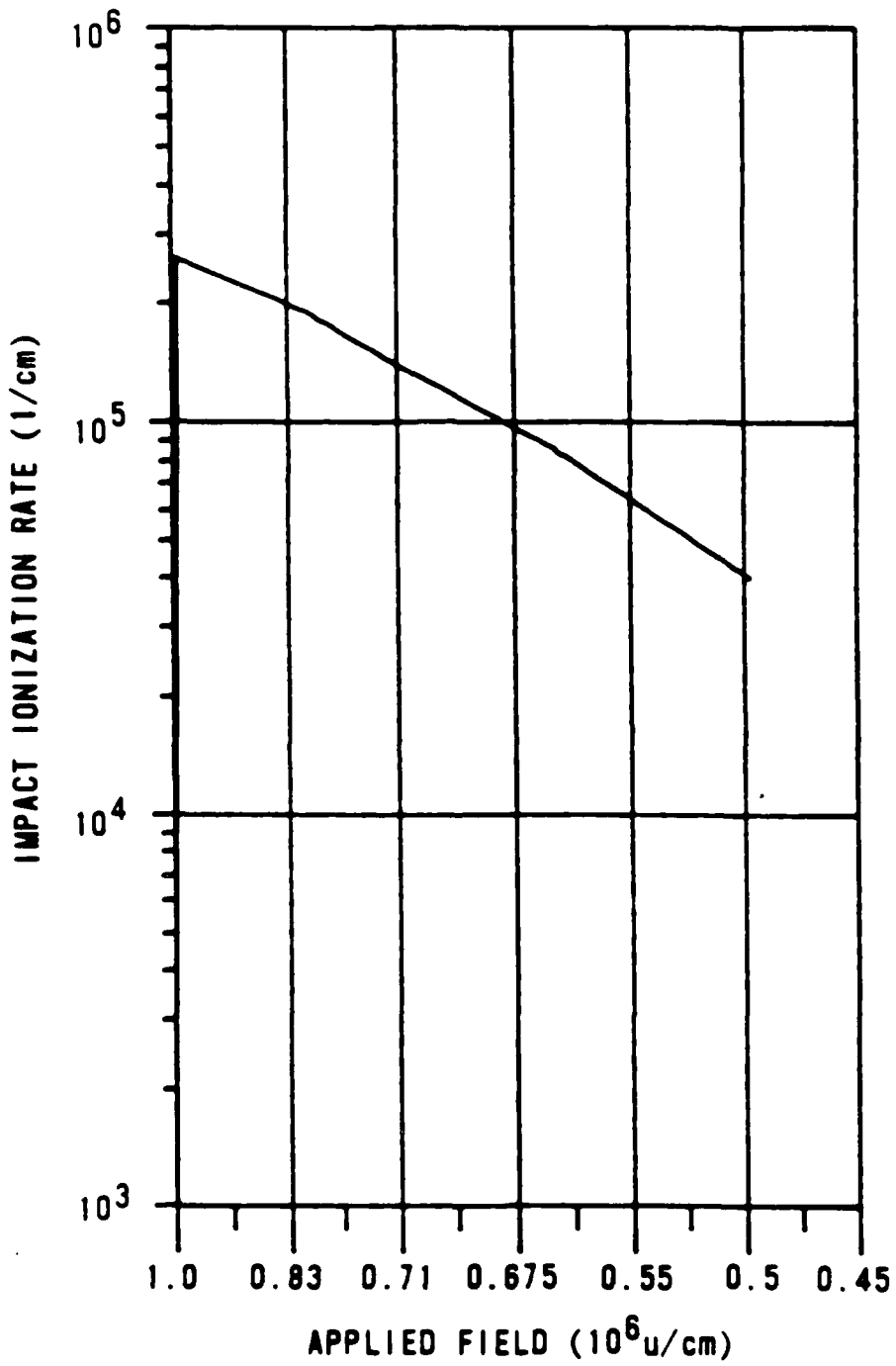


Figure A6. Impact ionization rate versus applied field in FaAs at $T = 800$ K. The coupling constant is 0.024.

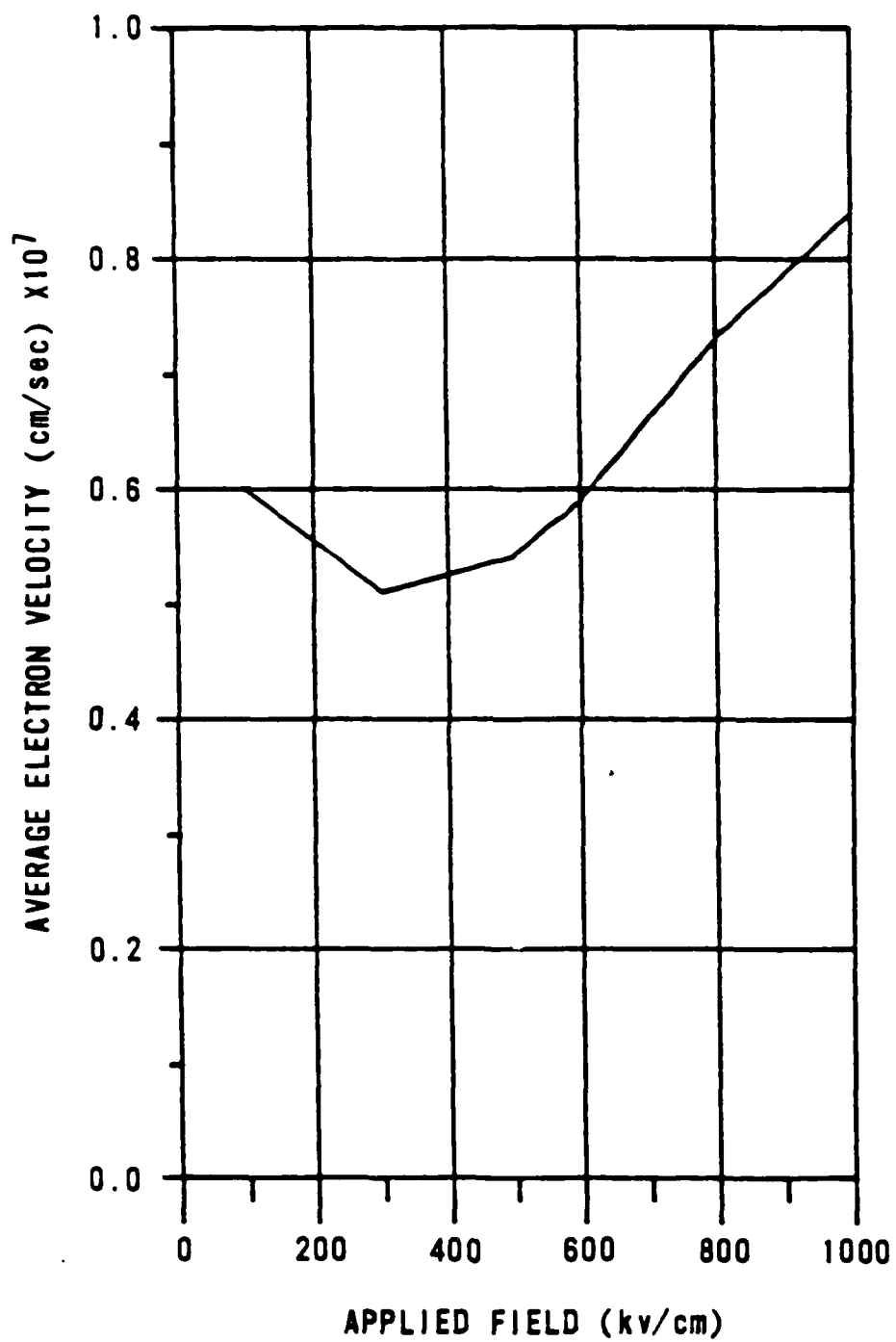


Figure A7. Average electron velocity versus applied field in GaAs at $T = 800$ K.

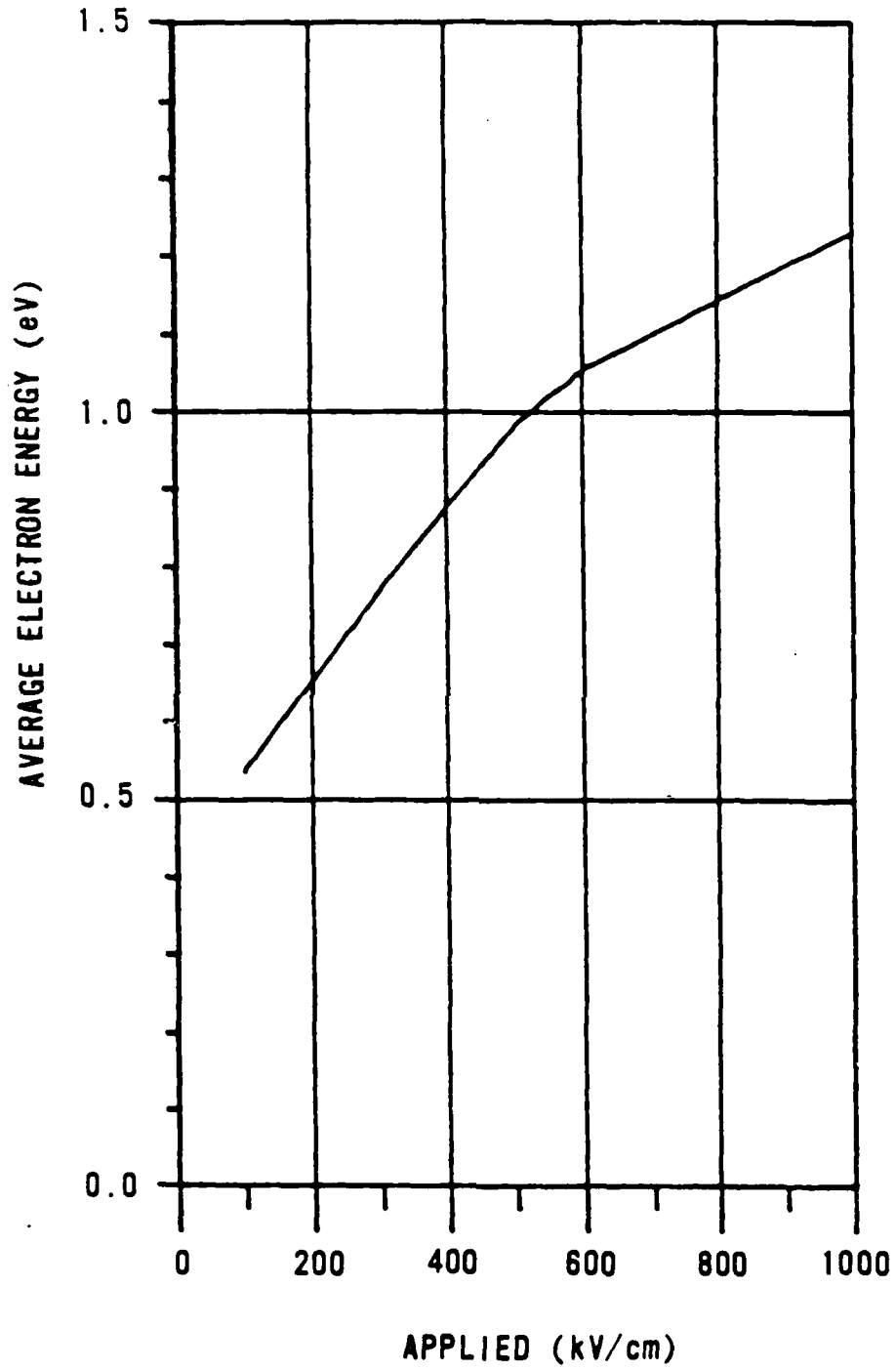


Figure A8. Average electron energy versus applied field for GaAs at T = 800 K.

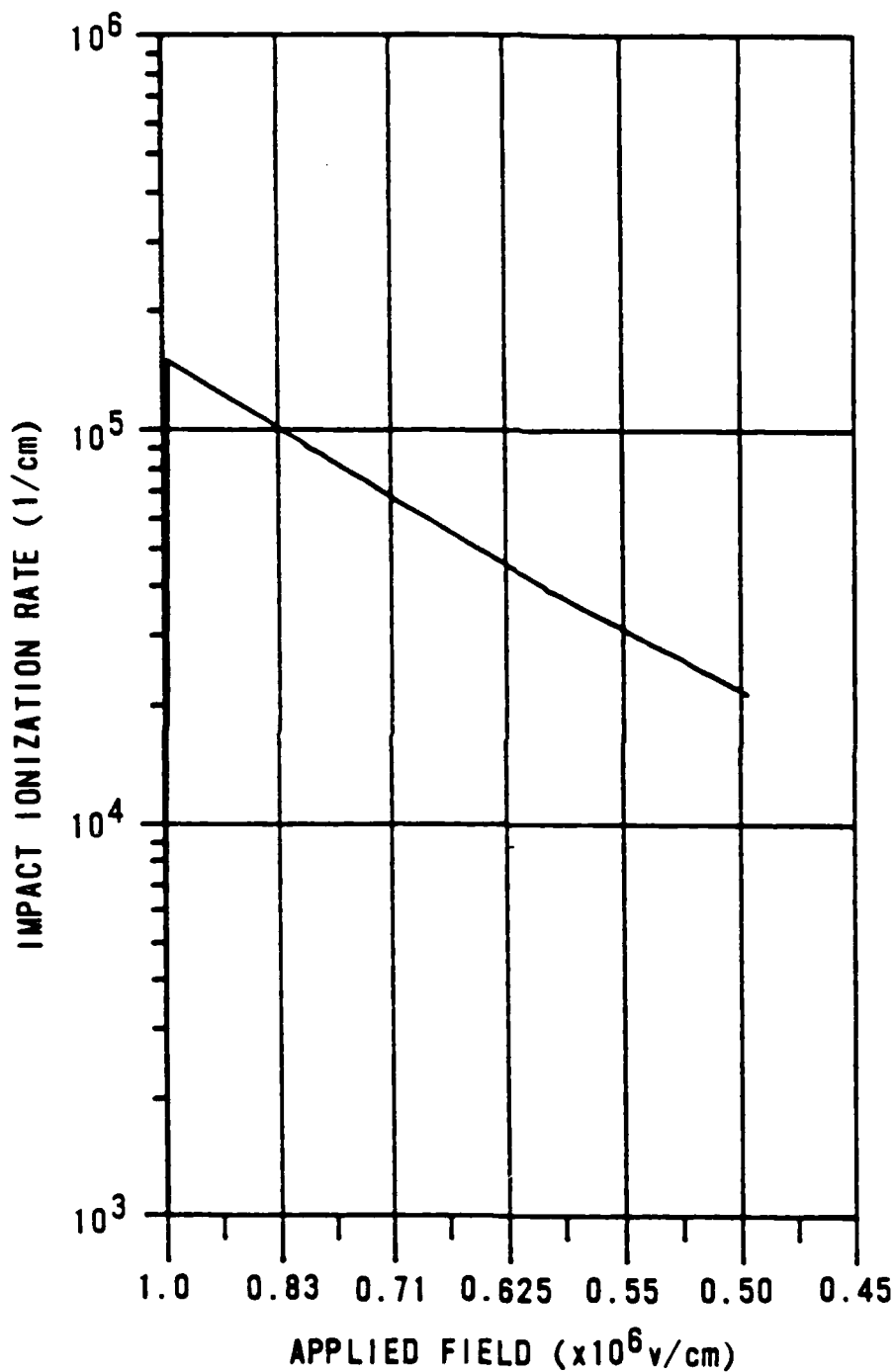


Figure A9. Impact ionization rate versus applied field for InP at $T = 300$ K. The coupling constant is 0.0273.

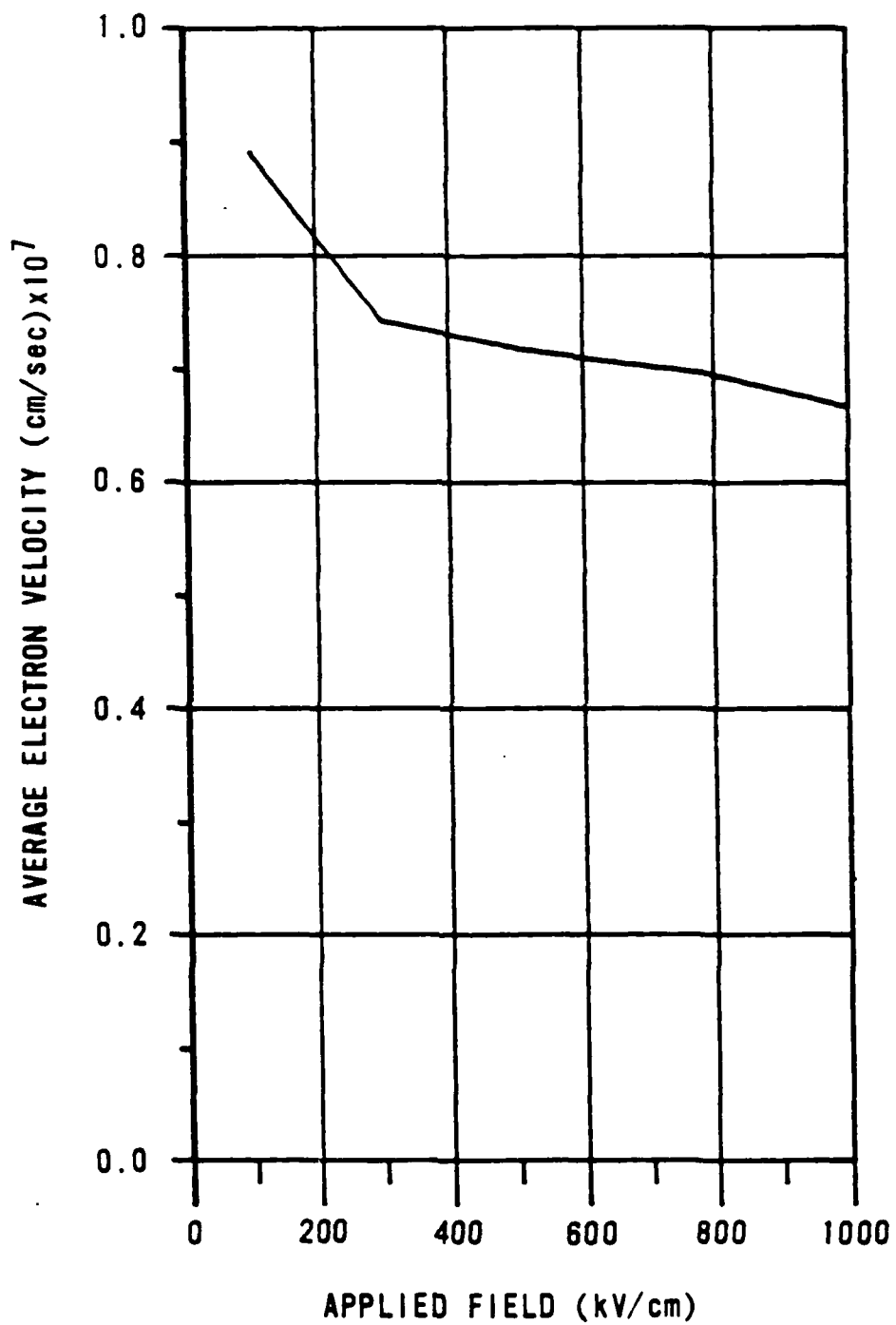


Figure A10. Average electron velocity versus applied field for InP at $T = 300$ K.

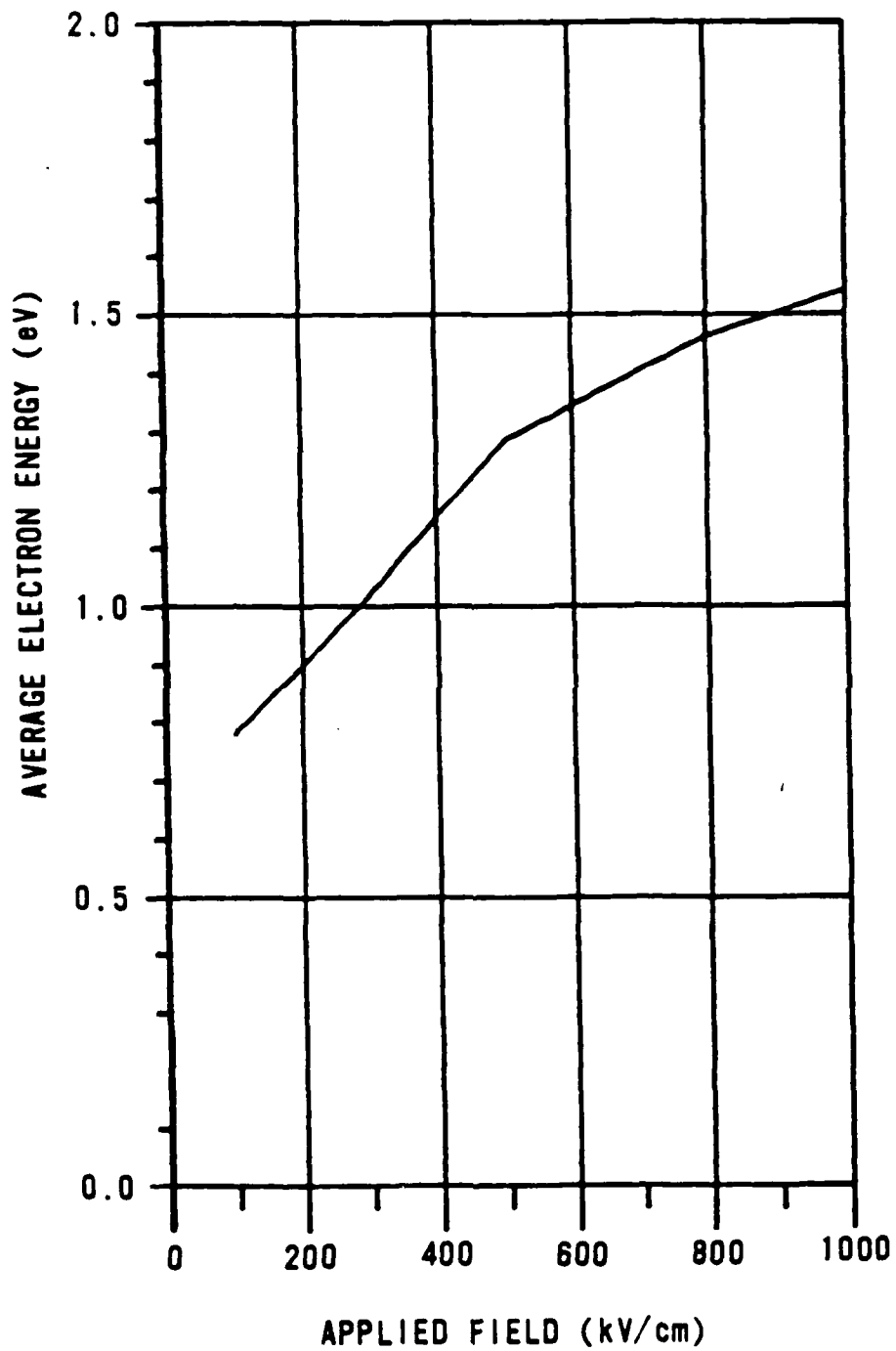


Figure A11. Average electron energy versus applied field in InP at $T = 300$ K.

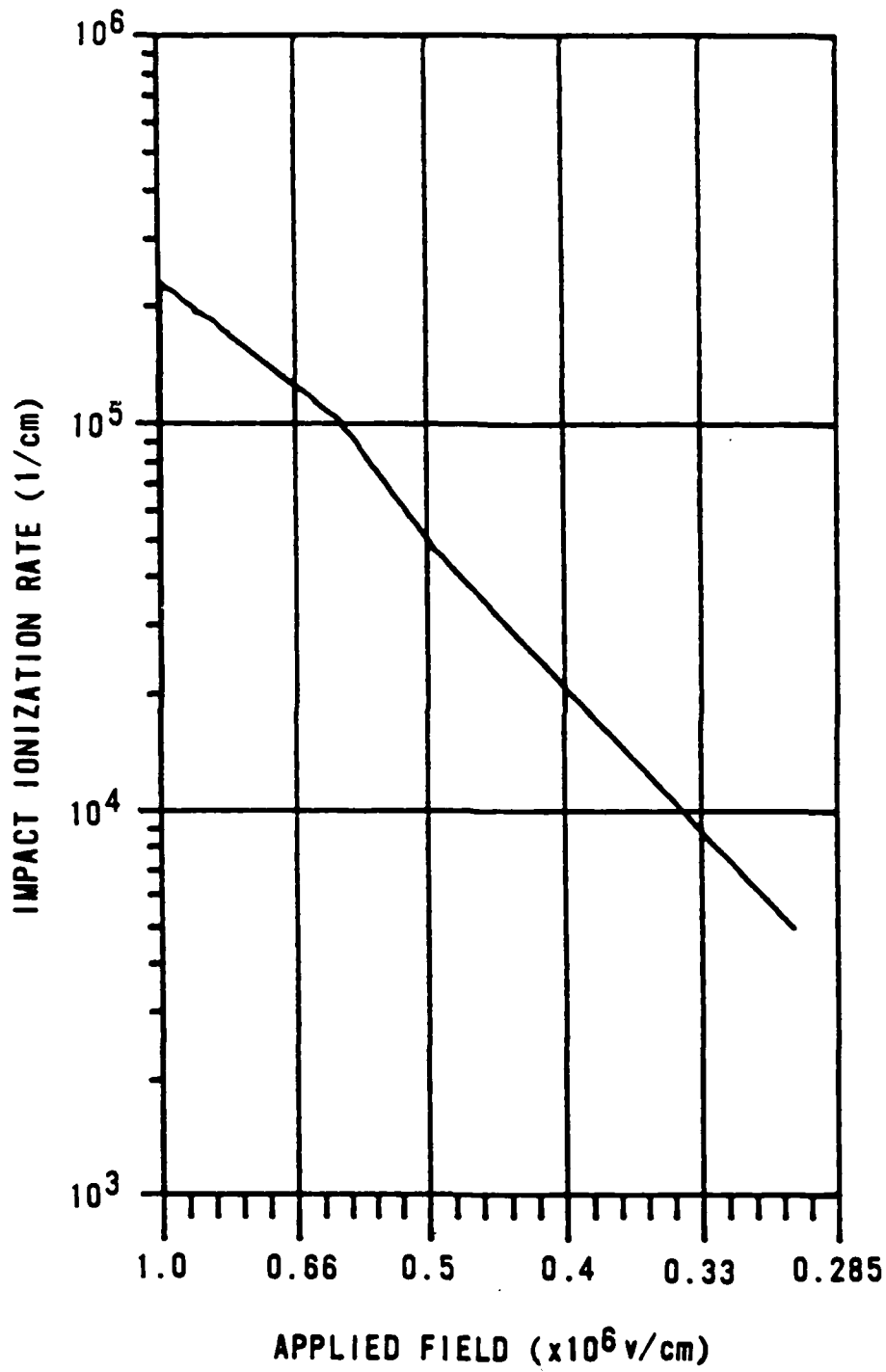


Figure A12. Impact ionization rate versus applied field for InP at $T = 500$ K. The coupling constant is unchanged.

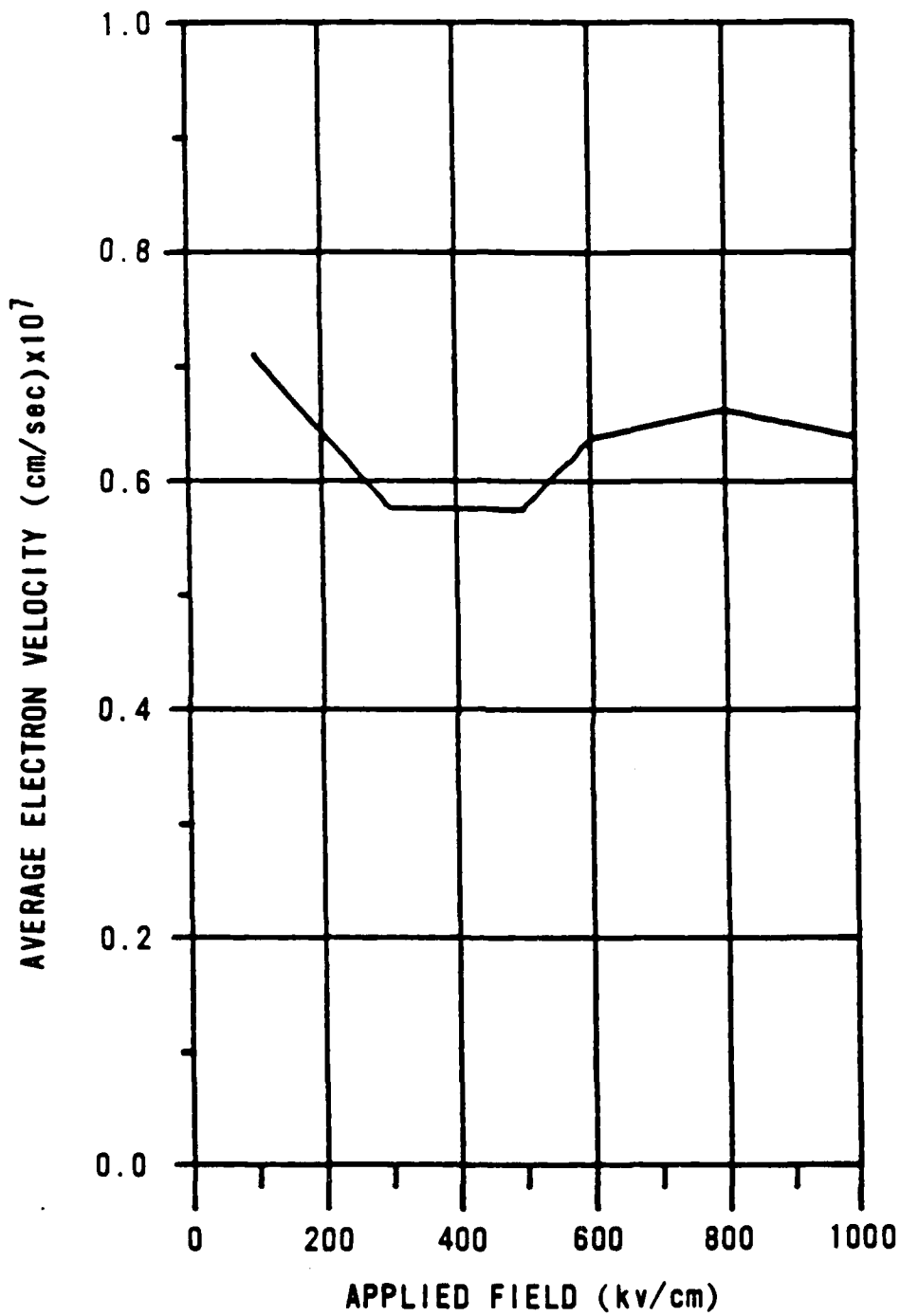


Figure A13. Average electron velocity versus applied field in InP at T = 500 K.

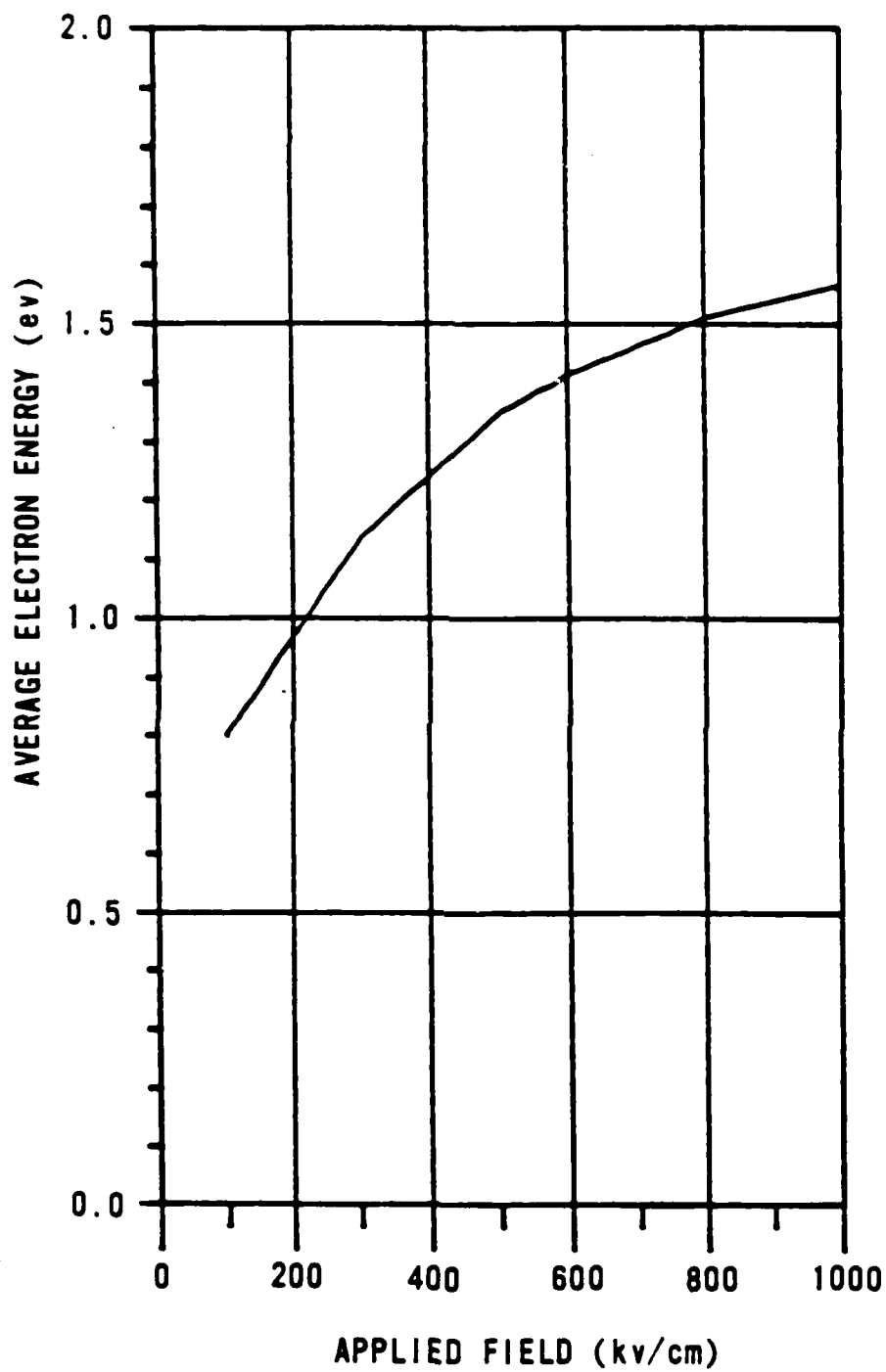


Figure A14. Average electron energy versus applied field in InP at T = 500 K.

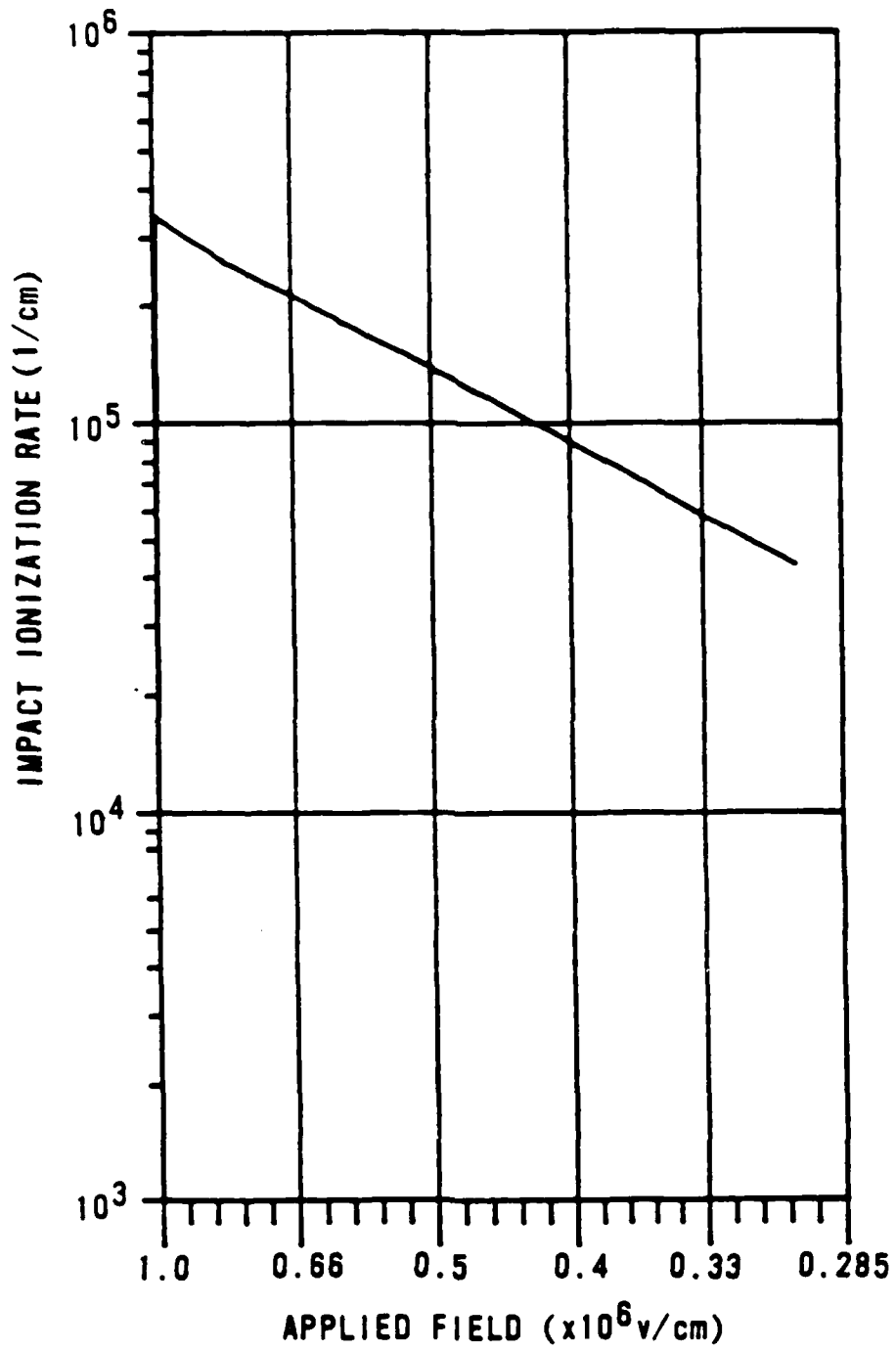


Figure A15. Impact ionization rate versus applied field in InP at $T = 800$ K. Coupling constant is unchanged.

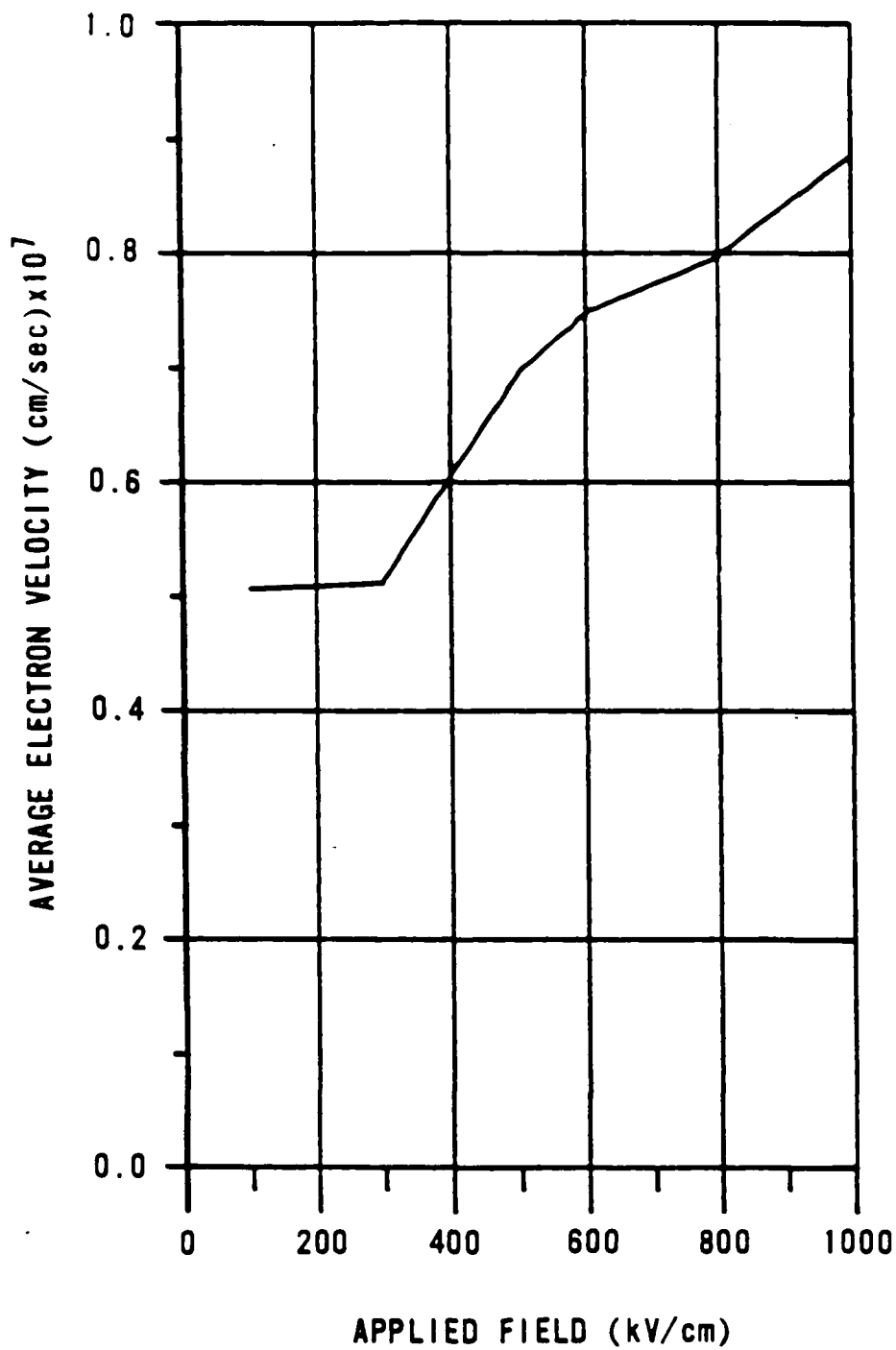


Figure A16. Average electron velocity versus the applied field in InP at T = 800 K.

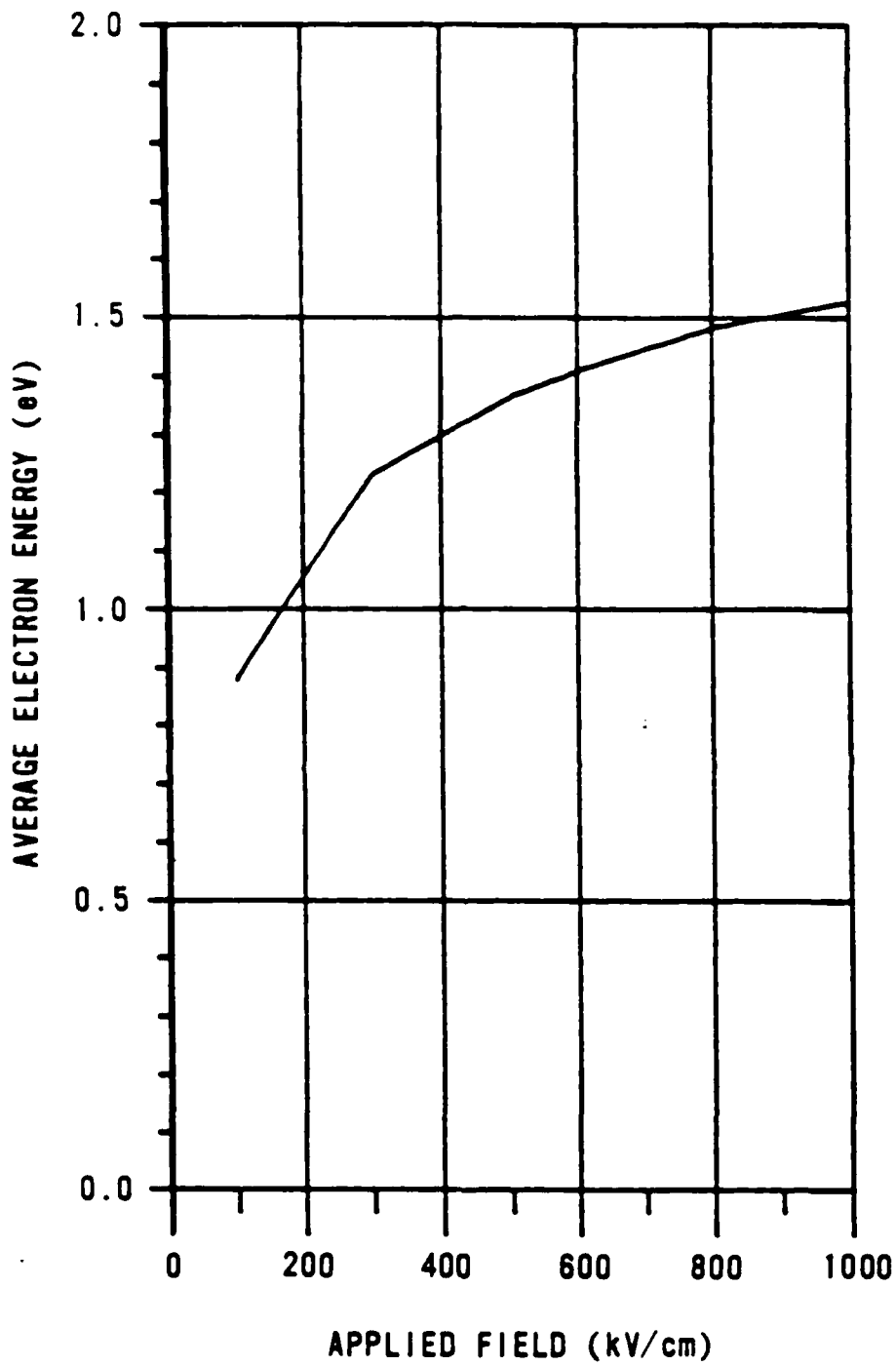


Figure A17. Average electron energy versus applied field in InP at T = 800 K.

END

8-87

DTIC